

Flight-Ready Precise and Robust Carrier-Phase GNSS Navigation Software for Distributed Space Systems

Samuel Y. W. Low, Toby Bell and Simone D'Amico

Stanford University, Department of Aeronautics and Astronautics, Space Rendezvous Laboratory

This paper presents the full requirements analysis, design, development, and testing of high-precision navigation flight software for Distributed Space Systems (DSS) using carrier phase differential GNSS. Five main contributions are made. First, a survey of flown and upcoming DSS missions with stringent precision requirements is conducted, from which a thorough requirements analysis is distilled to guide development and testing. Second, a real-time navigation functional architecture is designed, and adopts a sparse and regularized Consider Kalman Filter with options for numerical stability in-flight. The filter rigorously accounts for uncertainties in process noise, measurement noise, and biases. It tracks float ambiguities with integer resolution where possible. The covariance correlation structure is preserved under all navigation modes, including contingencies and outages. Third, a lightweight, memoryless Fault Detection, Isolation, and Recovery module is developed to guard against anomalous measurements, providing statistical screening and ensuring robust navigation. Fourth, the software architecture is proposed for ease of integration, with strategies presented for modularity and computational efficiency tailored to constrained flight systems. Fifth, a comprehensive test campaign is conducted, mapped to a requirements verification matrix, spanning unit, interface, software-in-the-loop, and real-time hardware-in-the-loop tests, emphasizing gradual test fidelity for efficient fault isolation. Finally, flight-like results are demonstrated using the VISORS mission, due to the generalizability of the VISORS navigation operations, and the stringency which demands sub-centimeter relative position and sub-millimeter-per-second velocity accuracy. This architecture aims to serve as a reference for next-generation DSS missions adopting CDGNSS.

Table of Abbreviations

CDGNSS	Carrier Phase Differential GNSS	CEKF	Consider Extended Kalman Filter	COM	Center of Mass
DDCP	Double Difference Carrier Phase	DSS	Distributed Space Systems	ECI	Earth-Centered Inertial Frame
EKF	Extended Kalman Filter	EOP	Earth Orientation Parameters	FDIR	Fault Detection, Isolation and Recovery
GRAPHIC	Group and Phase Ionospheric Calibration	IAR	Integer Ambiguity Resolution	PCO	Phase Center Offset
PCV	Phase Center Variations	RTN	Radial-Tangential-Normal Frame	SDCP	Single Difference Carrier Phase
STM	State Transition Matrix	UKF	Unscented Kalman Filter	ZDCP	Zero Difference Carrier Phase

I. Introduction

Precise relative navigation is a key enabler for emerging Distributed Space Systems (DSS), unlocking science not possible with monolithic spacecraft [1]. Distributed apertures, for instance, enable multi-static sensing, virtual telescopes, radio localization, gravimetry, and interferometry. Carrier Phase Differential GNSS (CDGNSS), often with Integer Ambiguity Resolution (IAR) [2], have seen increasing adoption in mission concept studies. Earlier missions like GRACE [3] and TanDEM-X [4] used post-processed batch CDGNSS with IAR on the ground. Recent advances support real-time onboard execution to meet stricter requirements [5]. PRISMA (2010) [6] demonstrated real-time onboard CDGNSS with Single Difference Carrier Phase (SDCP) float ambiguity estimation, achieving $\leq 5\text{cm}$ and 1mm/s baseline errors. Can-X 4/5 (2014) [7, 8] achieved $\leq 10\text{cm}$ in a CubeSat using an automotive-grade NovAtel OEMV-1G receiver. These missions serve as pathfinders for low-cost, high-impact science using CDGNSS. In future, the VISORS virtual telescope will employ L1-only CDGNSS with IAR for mm-level alignment across 40m baselines [9, 10], using a NovAtel OEM7 and laser rangefinder, for solar imaging. The mDOT star shade mission applies CDGNSS with differential ionospheric correction across 500km, for host starlight suppression and exoplanet detection [11–13]. Future pathfinders for spaceborne laser interferometry, like STARI [14] and SILVIA [15], propose to fuse CDGNSS with optical metrologies for micro-arcsecond imaging of exoplanets and black hole accretion disks. These missions, summarized in Table 1, serve as the foundation of our requirements analysis. The maturation of CDGNSS-based navigation parallels the growing availability and flight heritage of commercial-grade GNSS receivers, as seen in Can-X 4/5 [8] and VISORS [10]. CDGNSS has been studied for DSS for over two decades [16, 17], but adoption was initially hindered by costs and compute constraints. Today, new mission concepts leveraging CDGNSS continue to be proposed [14, 15, 18, 19],

as CDGNSS navigation architectures advance. One example is the *Distributed Multi-GNSS Timing and Localization* (DiGiTaL) flight software, which builds on PRISMA [6] and processes multi-GNSS measurements using a hybrid EKF-UKF architecture. DiGiTaL includes computational optimizations to the UKF that enable measurement updates every 30s with real-time onboard IAR—never before demonstrated in-flight [20, 21]. Sensor fusion with DiGiTaL has been explored using vision-based angles-only measurements at far-range and image-based pose estimation at close-range [22]. Tight coupling of angles-only and range measurements within the integer search process has demonstrated improved IAR accuracy in noisy environments, potentially enabling IAR in HEO/GEO sidelobe-only scenarios [23]. For the N -spacecraft case, scalability of the software has been explored briefly [21], and search-based optimization of attitude pointing profiles have been proposed to support such navigation ops in larger swarms [24].

Table 1 Survey of contemporary distributed space missions exploiting GNSS for precision applications

Year	Mission	Mass [kg]	Purpose	Orbit	Baseline	Methodology	Accuracy
2002	GRACE [3]	487×2	Gravimetric Modeling	Polar LEO, 500km	170 to 270km	Ground post-processed CDGNSS with IAR, with K-Band range aiding	$\sim 1\text{mm}$
2010	TanDEM-X [4]	1230 & 1330	InSAR & Elevation Mapping	Polar LEO, 514km	250 to 500m	Ground post-processed CDGNSS with IAR, with ground satellite laser ranging	$\sim \text{cm}$
2010	PRISMA [6, 25]	150 & 40	Formation Flying Demo	LEO, 700km	100m to 2km	Real-time onboard CDGNSS float ambiguity estimation	$\leq 10\text{cm}$
2014	Can-X 4/5 [7, 8]	6.5×2	Formation Flying Demo	Polar LEO, 650km	50m to 1km	Real-time onboard CDGNSS float ambiguity estimation	$\leq 10\text{cm}$
2018	GRACE-FO [26, 27]	600×2	Gravimetric Modeling	Polar LEO, 490km	220km	Ground post-processed CDGNSS with IAR, with onboard laser interferometry	$\leq 1\text{mm}$
2022	CPOD [28, 29]	4.5×2	RPOD Tech Demo	LEO, $\sim 500\text{km}$	361m to 997km	Real-time onboard fusion of GPS pseudorange with crosslink range and camera measurements	$\sim \text{meters}$
2024	PROBA-3 [30–32]	340 & 200	Distributed Telescopy	HEO, 600 to 60,530km	200m to 2km	Ground post-processed GNSS at perigee; laser ranging, vision and shadow position sensors at apogee	$\sim \text{mm}$
~ 2026	VISORS [9, 10]	10 & 11	Distributed Telescopy	Polar LEO, 500 - 600km	40 to 200m	Real-time onboard CDGNSS with IAR, with laser ranging during observations	$\sim \text{mm}$
~ 2027	SNUGLITE III [19, 33, 34]	3.6×2	GPS-RO and Tech Demo	SSO, 500–600km	$\leq 1\text{km}$	CDGNSS with IAR, GPS-only attitude determination, drag-only control	$\sim \text{mm}$
Proposed	mDOT [11–13]	246 total	Exoplanet Detection	LEO, $\sim 500\text{km}$	500km	Real-time onboard CDGNSS with IAR	$\sim \text{mm}$
Proposed	STARI [14]	10×2	Interferometry Demo	LEO, $\sim 500\text{km}$	10 to 100m	Real-time onboard CDGNSS with IAR, possibly aided by LED-based image alignment measurements	$\sim \text{mm}$
Proposed	SILVIA [15]	100×3	Interferometry Demo	LEO, 500 - 600km	$\sim 100\text{m}$	Float-only CDGNSS (precise mode), laser and beam position sensors (ultra-precise)	$\sim \text{mm} - \mu\text{m}$

Despite advances in CDGNSS-based navigation, challenges persist. Emerging missions such as VISORS [9, 10], mDOT [12, 13], and STARI [14] demand unprecedented accuracy and robustness yet have not achieved the required performance [35]. A key gap in literature is the absence of an end-to-end architecture that: (i) generalizes to future DSS missions, (ii) rigorously models state, measurement, and dynamic uncertainties under off-nominal conditions, (iii) ensures robustness to navigation errors and software faults, (iv) remains computationally efficient for frequent measurement updates in flight, and (v) closes the requirements loop through comprehensive testing. This work formalizes a DiGiTaL v2 flight software to address these gaps. Section I reviews relevant missions for a generalizable requirements analysis. Section II refines requirements into Interfacing, Functional, and Performance categories. Section III presents a filter design that rigorously treats state, dynamics, and measurement uncertainty, introducing a regularized Joseph-like Consider Kalman Filter. Section IV integrates a lightweight, memoryless FDIR module leveraging statistical guarantees to handle anomalies such as undetected carrier phase cycle slips. Section V details a modular, compute-optimized software architecture with full execution logic. Section VI outlines a structured, requirements-driven test campaign spanning unit to real-time GNSS hardware-in-the-loop tests, demonstrated using the VISORS mission concept. The VISORS campaign is chosen as it generalizes to future DSS missions and establishes a benchmark for flight software evaluation. State-of-the-art models for dynamics, measurements, subsystem latencies, and body-frame uncertainties are incorporated. Overall, this work delivers a traceable, closed-loop framework from requirements to compliance testing, advancing the readiness of CDGNSS-based navigation for next-generation DSS missions.

II. Navigation Requirements

A. Requirements Generalizations and Assumptions

This section presents a generalized set of CDGNSS-based navigation requirements catered to a set of generalized operating modes applicable to missions surveyed. Clearly defined requirements are essential for guiding design decisions, ensuring validation, and avoiding costly issues later in development lifecycle [36]. The first necessary assumption made is that the spacecraft in question are cooperative, communicable, and operating under main-lobe GNSS reception. For guidance, a general DSS mission may adopt the following modes in Figure 1,

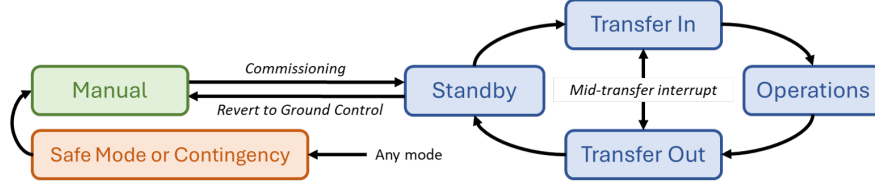


Fig. 1 Generalized *modes* that spacecraft in a distributed system may adopt.

A *mode* is a logical abstraction of a spacecraft's current state meant to fulfil objectives or situational needs at each phase of the mission. With regards to software, different modes can adopt different configuration parameters and tailor compute resources to each phase of the mission. With regards to ops, different modes are often also characterized by different operating baselines, relative orbital elements, and passive safety margins [37]. The purpose of the abstraction in Figure 1 is to provide a context in which we present requirements, and cater them in accordance to the generalized stringency of each mode. Broadly, Standby mode is purposed for subsystem health monitoring and software checkouts prior to Transfer, which is a relative orbit reconfiguration trajectory, into Operations, which is purposed for execution of the payload. Generally, navigation accuracy requirements and passive safety margins are most stringent during Operations, and less so during Standby. The transition between Manual to and from Standby also imposes unique requirements on the handling of mode transitions and performance, if the DSS is in acquisition or recovery (where the CDGNSS may not be available). Such mode-based operations mirror that seen in several recent or proposed missions such as VISORS [9, 10], mDOT [12, 13], and PROBA-3 [30].

B. Requirements Identification

This survey of contemporary and emerging distributed space missions Table 1 forms the foundation for identifying navigation flight software requirements that are both mission-relevant and broadly generalizable. By analyzing commonalities across mission objectives, operating baselines, and CDGNSS-based navigation methodologies, a unified set of requirements was distilled to guide the design of a robust and adaptable navigation architecture.

Requirements are segmented into Interfacing, Functional, and Performance in Table 4. The specification of interface and functional requirements implicitly assume an interface architecture depicted in Figure 2. Such a prescribed interface has been adopted for several missions that employ CDGNSS, such as PRISMA [1], Can-X 4/5 [7] [8], DWARF [38]. It is generalizable to future missions such as VISORS [10] and STARI [14] as well.

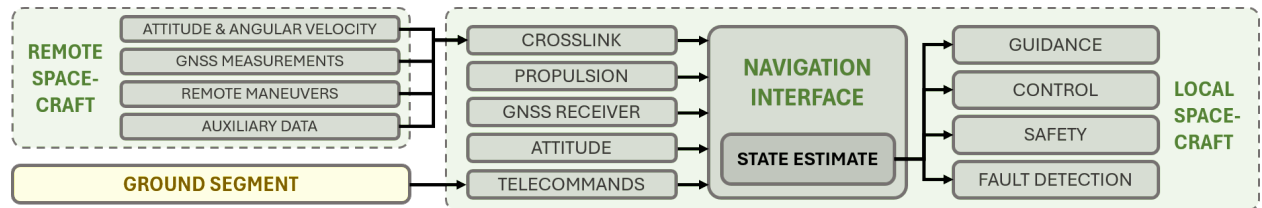


Fig. 2 Assumed interface architecture applied in the context of identifying interface requirements.

The specification of performance requirements are segmented according to the types of navigation operations in Figure 3. These are derived from navigation requirements from each mode of Figure 1. The line mappings are a suggestive (and not prescriptive) indication on whether requirements for each form of navigation operation are being driven by mode requirements.

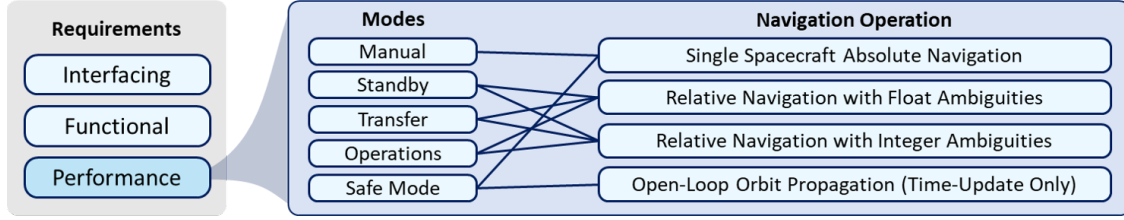


Fig. 3 Mapping of navigation operating requirements to the spacecraft modes

	Interfacing Requirements	Parameter
R1.1	Local GNSS: Provide an interface for receiving local GNSS measurements at intervals τ_{meas} , GNSS ephemeris at intervals ≤ 2 hours, and receiver health data, with validation via checksums.	τ_{meas}
R1.2	Local Attitude: Provide an interface for receiving local attitude at intervals τ_{att} . If no angular velocity provided for propagation, then ≥ 2 attitude states are to be buffered for inter/extrapolation over short arcs.	τ_{att}
R1.3	Local Propulsion: Provide an interface for receiving time-tagged local spacecraft maneuver plans to be buffered and applied during navigation filter time updates.	-
R1.4	Crosslink In/Out: Provide an interface for receiving crosslink <i>from</i> the remote spacecraft (and <i>to</i> , if the remote also executes onboard navigation), at intervals τ_{link} , with validation via checksums. Crosslink packets may include GNSS measurements, attitudes, maneuver plans, status bytes, and state estimates.	τ_{link}
R1.5	Ground Segment: Provide an interface for receiving ground tele-commands <i>e.g.</i> filter configurations, and auxiliary data such as GPST leap seconds and Earth Orientation Parameters (EOPs).	-
R1.6	Outputs: Provide an interface to return or call-back to the host software with state estimates at intervals τ_{update} . If state estimates are anomalous, an incapability flag with status bytes should be returned instead.	τ_{update}
	Functional Requirements	
R2.1	State Covariance: Maintain the state estimate with a <i>positive-definite</i> covariance matrix that is reflective of the true state errors.	-
R2.2	State Dynamics Fidelity: Filter dynamics must provide sufficient fidelity in orbit perturbations without exceeding the margin of compute resources <i>i.e.</i> the filter time update and measurement update can be still be completed within τ_{update} , tested on a representative flight computer.	-
R2.3	Screening for Data Health: The flight software shall... <ul style="list-style-type: none"> • Reject measurements with poor C/N_0 ratios. A recommended minimum value is 45 dB-Hz [39]. • Reject local/remote maneuvers and measurements with outdated time-tags, with respect to filter time. • Reject observed ranges and range rates with impossible magnitudes that lie outside expected bounds. • Reject stale GNSS ephemerides (≥ 2 hours) or with bad Keplerian elements (<i>e.g.</i> negative eccentricity). • Reject bad attitude state representations <i>e.g.</i> quaternions which violate unit norm constraints, and emit warning flags if attitudes received are not indicative of the pointing profile in the current mode. 	-
R2.4	Managing Telecommands and Telemetry: Navigation remains uninterrupted during telecommand uplink (<i>e.g.</i> filter tuning parameters, leap-second update, or new EOPs), and telemetry downlink.	-
R2.5	Managing Mode Switches: Navigation remains uninterrupted in the event of a system-wide role or mode switch. A handshake should be conducted between instances of the navigation flight software onboard and with remote spacecraft, if necessary, to prevent role or mode inconsistencies across the formation.	-
R2.6	Managing Measurement Latency: Provide a decision logic for transitioning to local-only spacecraft absolute state estimation, if an extended outage from the remote crosslink is experienced beyond some time horizon τ_{outage} . A decision logic for recovery back to precise relative state estimation should also be provided.	τ_{outage}
R2.7	Managing Attitude Latency: Propagate body-to-inertial attitude coordinates to the time-tag of the measurements at filter updates. If angular velocities are absent, perform inter/extrapolation instead [40].	-
R2.8	Fault Detection in Computations: Design against numerical instabilities. Automated unit tests are recommended. Catch problems involving potential divisions by zero, negative eccentricities, square roots of negative real numbers, integer over/underflow, precision loss and ill-conditioned matrices. Conversions of units, state representations, coordinate frames, time units and time scales must be verified.	-

R2.9	Cycle Slip Detection: Provide a mechanism for screening cycle slips (if the receiver does not already provide cycle slip flags), and provide a remedy if slip exists. Recommended techniques in literature include (i) consistency checks between the carrier phase and Doppler measurements, (ii) detection of discontinuities in double-differenced carrier phase, or (iii) impulses in triple-differenced carrier phase [39].	-
Performance Requirements		
R3.1	Absolute Navigation: Maintain a single-point positioning 1σ error of $\leq e_{abs}$ m and \dot{e}_{abs} m/s.	e_{abs}, \dot{e}_{abs}
R3.2	Relative Navigation (Pre-IAR): Maintain a relative positioning 1σ error of $\leq \delta e_{float}$ m and $\delta \dot{e}_{float}$ m/s at convergence of estimated single-differenced float ambiguities.	$\delta e_{float}, \delta \dot{e}_{float}$
R3.3	Relative Navigation (Post-IAR): Maintain a relative positioning 1σ error of $\leq \delta e_{iar}$ m and $\delta \dot{e}_{iar}$ m/s of single-differenced integer ambiguities using a $\geq 99\%$ probability of success metric.	$\delta e_{iar}, \delta \dot{e}_{iar}$
R3.4	Relative Navigation (Operations): In addition to R3.1 - R3.3, instrument or payload alignment requirements may be imposed along the longitudinal boresight axis of the instrument, or across the lateral plane perpendicular to the longitudinal, or both, given as the 1σ error δe_{lon} and δe_{lat} .	$\delta e_{lon}, \delta e_{lat}$
R3.5	Open-Loop Orbit Propagation: If state updates are necessary during measurement outages, then the open-loop propagation of the relative trajectory must be within an error tolerance of δe_{open} in the time horizon τ_{open} .	$\delta e_{open}, \tau_{open}$
R3.6	Robustness to Offset-from-Origin Biases: If there exists a poorly observable bias \vec{p} , between the chosen origin of the spacecraft body frame and the GNSS antenna phase center, then the performance requirements must be tolerant to the knowledge error of this bias given by $\Delta \vec{p}_{req}$.	$\Delta \vec{p}_{req}$
R3.7	Robustness to Over/Under-Actuation Maneuvers: Requirements R3.1 - R3.5 must remain satisfied in the event of over or under-actuation between the known maneuvers and true executed maneuvers up to some margin M_{man} .	M_{man}
R3.8	Robustness to Measurement Noise Variations: Requirements R3.1 - R3.5 must remain satisfied in the event of variations between modeled and actual measurement noise up to some margin M_{meas} . This variation is to be tested using a representative receiver under noise-configurable emulated GNSS signals.	M_{meas}

Table 4 Identified requirements of a generalized CDGNSS-based navigation flight software for DSS missions.

Deciding on the Interfacing and Functional requirement parameters in Table 4 may depend on the mission context and domain knowledge of other subsystems interfacing with navigation. τ_{meas} is limited by available observation rate of the GNSS receiver; τ_{att} is limited by the bus ADCS; τ_{link} is limited by crosslink availability; τ_{outage} requires domain knowledge on the expected crosslink latency; and while τ_{update} can be set as an ops requirement, it is also limited by τ_{meas} and τ_{link} . Deciding on the Performance requirements parameters requires a careful assessment of the navigation error tolerance necessary to meet mission-specific requirements. An example of requirements parametrization is drawn from the VISORS mission: critical considerations for science observations are the focal length control accuracy, image drift rate, and attitude pointing accuracies, all during telescopic alignment. The science requirement is $\geq 20\%$ likelihood of success per observation attempt, and hence $\sim 99\%$ likelihood of ≥ 1 successful observation after 20 attempts [9, 10]. In total, these translate into overall Interfacing and Functional requirements parameters in Table 5 and Performance requirements parameters in Table 6, specific to the VISORS mission:

Table 5 Interfacing and Functional requirements drawn from the VISORS Navigation Flight Software

τ_{meas}	τ_{att}	τ_{link}	τ_{update}	τ_{outage}
10s	10s	10s	10s	4s

Table 6 Performance Requirements drawn from the VISORS Navigation Flight Software

\vec{e}_{abs}	$\dot{\vec{e}}_{abs}$	$\delta \vec{e}_{float}$	$\delta \dot{\vec{e}}_{float}$	$\delta \vec{e}_{int}$	$\delta \dot{\vec{e}}_{int}$	δe_{lon}	δe_{lat}	δe_{open}	τ_{open}	$\Delta \vec{p}_{req}$	M_{man}	M_{meas}
5m	5mm/s	10cm	1mm/s	1cm	100 μ m/s	1.5cm	1.75cm	1m	1 orbit	5cm	$\pm 100\%$	$\pm 300\%$

III. Navigation Functional Architecture

A. Overview of Architecture

The navigation architecture builds on the DiGiTaL flight software [20, 21], with heritage from PRISMA [6, 25], and is hereafter referred to as DiGiTaL v2. Absolute position estimation uses Group and Phase Ionospheric Calibration (GRAPHIC) measurements [50], which combine pseudorange and Zero-Difference Carrier Phase (ZDCP) to mitigate ionospheric errors. Relative baseline estimation uses Single-Difference Carrier Phase (SDCP) measurements shared over a crosslink. The architecture in Figure 5 comprises four blocks: (i) the data interface, (ii) navigation filter, (iii) IAR, and (iv) FDIR.

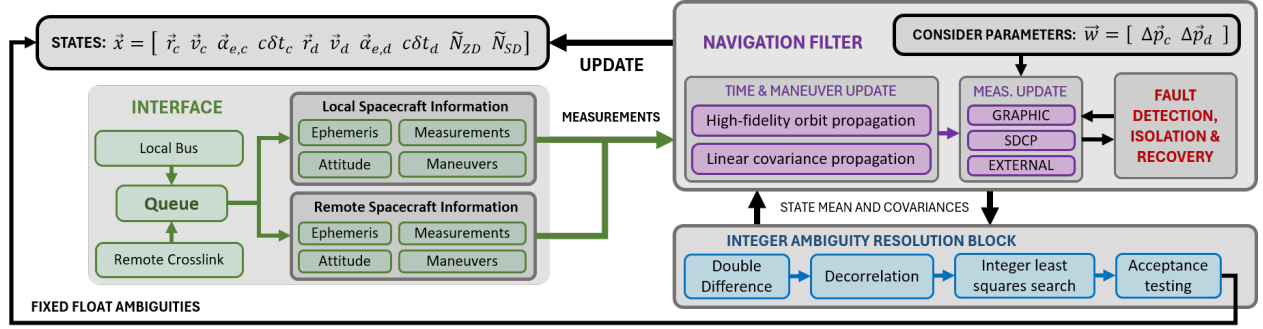


Fig. 5 Navigation functional architecture based on CDGNSS with IAR, for a two-spacecraft state vector

The state vector per spacecraft contains the inertial position \vec{r}_i and velocity \vec{v}_i of the spacecraft COM, empirical accelerations $\vec{a}_{e,i}$, and receiver clock offsets $c\delta t_i$. 48 channels total are set for estimating ZDCP and SDCP float ambiguities \tilde{N}_{ZD} and \tilde{N}_{SD} . Receiver clock offsets and empirical accelerations are modeled temporally as first-order Gauss-Markov processes.

$$\vec{x} = [\vec{r}_c, \vec{v}_c, \vec{a}_{e,c}, c\delta t_c, \vec{r}_d, \vec{v}_d, \vec{a}_{e,d}, c\delta t_d, \tilde{N}_{ZD}, \tilde{N}_{SD}] , \quad \vec{w} = [\Delta \vec{p}_c, \Delta \vec{p}_d] , \quad \Sigma = \begin{bmatrix} \Sigma^{(x)} & \Sigma^{(xw)} \\ \Sigma^{(wx)} & \Sigma^{(w)} \end{bmatrix} \quad (3)$$

For a two-spacecraft formation (chief c and deputy d), the state mean and consider parameters have dimensions $\vec{x} \in \mathbb{R}^{68}$ and $\vec{w} \in \mathbb{R}^6$. The full covariance block matrix, including consider parameters, comprises the state covariance $\Sigma^{(x)}$; consider covariance $\Sigma^{(w)}$; and cross-covariances between states and consider parameters $\Sigma^{(xw)} = \Sigma^{(wx)\top}$. Ambiguities are indexed to the rear in Equation 3 to allow for further computational optimization as shown in Section V.

B. Stable and Regularized Consider Extended Kalman Filter

The Consider Extended Kalman Filter (CEKF) propagates the uncertainties of $\Delta \vec{p}_c, \Delta \vec{p}_d$ into the state covariance [46, 47]. However, the standard minimum covariance form [48] can pose numerical stability issues, detrimental to real-time flight. The key contribution in this section is the modification of the CEKF into a Positive-Definite (PD) preserving Joseph form [51], with regularization of the innovation covariance for additional stability. Modifications are in Equation 14 and Equation 20. The time update equations span from Equation 4 to Equation 8. Let f be the non-linear orbit propagation force model, where $\dot{\vec{x}} = f(t, \vec{x}, \mathbf{M})$ includes higher order perturbations; $\mathbf{M} \in \mathbb{R}^{r \times 3}$ is a maneuver buffer of size r ; Φ_{t-1} is the State Transition Matrix (STM) at time $t-1$; and \mathbf{Q}_t is the process noise matrix at time t . Then,

$$\vec{x}_{t|t-1} = \text{Propagate}(t, \vec{x}_{t-1|t-1}, \mathbf{M}, f) \quad (4)$$

$$\Sigma_{t|t-1}^{(x)} = \Phi_{t-1}^\top \Sigma_{t-1|t-1}^{(x)} \Phi_{t-1} + \mathbf{Q}_t \quad (5)$$

$$\Sigma_{t|t-1}^{(xw)} = \Sigma_{t|t-1}^{(wx)\top} = \Phi_{t-1}^\top \Sigma_{t-1|t-1}^{(xw)} \quad (6)$$

Empirical accelerations are decayed based on a first-order Gauss-Markov [1, 21, 45, 52]. Attitudes are propagated to match the filter time, so as to minimize residuals from uncompensated rotations of the COM-to-PCO lever-arm,

$$\vec{\alpha}_{e,i} = \vec{\alpha}_{e,i} \cdot e^{-\Delta t/\tau_{ae}}, \quad \forall i \text{ spacecraft} \quad (7)$$

$$\mathbf{q}(t) = \delta \mathbf{q} \otimes \mathbf{q}(t_{att}), \quad \text{see Equation 2} \quad (8)$$

where $\mathbf{q}(t_{att})$ is the last known attitude at ADCS time t_{att} . Attitude time-tags t_{att} marked by the ADCS must also be converted to the same time scale as the filter. An analytical form of Φ_{t-1} is difficult to achieve in practice, and hence the STM can be approximated via the variational equations so as to capture perturbations of f through the STM. This is reviewed in Ch.7 of Montenbruck and Gill [53]. For example, given a state transition through time $t_0 \rightarrow t$ in position-velocity space $\Phi_{rv}(t, t_0)$, and given the Jacobian \mathbf{F} of the force model f with respect to \vec{r}, \vec{v} , the variational equations provide the STM rate of change:

$$\frac{d}{dt} \Phi_{rv}(t, t_0) = \mathbf{F}(t) \cdot \Phi_{rv}(t, t_0), \quad \text{where} \quad \mathbf{F}(t) = \begin{bmatrix} \mathbf{0}_{3 \times 3} & \mathbf{I}_{3 \times 3} \\ \frac{\partial f(\vec{r}, \vec{v}, t)}{\partial \vec{r}(t)} & \frac{\partial f(\vec{r}, \vec{v}, t)}{\partial \vec{v}(t)} \end{bmatrix}_{6 \times 6} \quad (9)$$

The partial derivatives in $\mathbf{F}(t)$ are approximated using difference quotients rather than solved analytically. By the variational equations of Equation 9 we can obtain the example STM $\Phi_{rv}(t, t_0)$ by propagating the initial condition $\Phi_{rv}(t_0, t_0) = \mathbf{I}_{6 \times 6}$. Similarly, numerical difference quotients are used to evaluate partial derivatives within the sensitivity $\Phi_{rv,\alpha}(t)$ of the position-velocity states with respect to empirical accelerations,

$$\frac{d}{dt} \Phi_{rv,\alpha}(t) = \mathbf{F}(t) \cdot \Phi_{rv,\alpha}(t) + \mathbf{G}(t), \quad \text{where} \quad \mathbf{G}(t) = \begin{bmatrix} \mathbf{0}_{3 \times 3} \\ \frac{\partial f(\vec{r}, \vec{v}, \vec{\alpha}_e, t)}{\partial \vec{\alpha}_e} \end{bmatrix}_{6 \times 3} \quad (10)$$

where the initial condition of the sensitivity $\Phi_{rv,\alpha}(t_0) = \mathbf{0}_{6 \times 3}$. Since empirical accelerations follow a first order Gauss Markov process modelled by a decaying transition with a correlation time constant τ_{ae} , their STM is simply $\Phi_\alpha = \text{diag}[\phi_R, \phi_T, \phi_N]_{3 \times 3}$ and $\phi_k = e^{-(t-t_0)/\tau_{ae}}$ for $k \in [R, T, N]$. Empirical accelerations are assumed independent across the Radial-Tangential-Normal (RTN) axes of the spacecraft. For the full filter state, superscripts (i) and (j) indicate each spacecraft. The total STM involving positions, velocities and empirical accelerations for both spacecraft is the concatenation given in Equation 11,

$$\Phi_{rv\alpha} = \begin{bmatrix} \Phi_{rv\alpha}^{(i)} & \mathbf{0}_{9 \times 9} \\ \mathbf{0}_{9 \times 9} & \Phi_{rv\alpha}^{(j)} \end{bmatrix}, \quad \text{where} \quad \Phi_{rv\alpha}^{(i)} = \begin{bmatrix} \Phi_{rv}^{(i)} & \Phi_{rv,\alpha}^{(i)} \\ \mathbf{0}_{3 \times 6} & \Phi_\alpha^{(i)} \end{bmatrix} \quad \text{and} \quad \Phi_{rv\alpha}^{(j)} = \begin{bmatrix} \Phi_{rv}^{(j)} & \Phi_{rv,\alpha}^{(j)} \\ \mathbf{0}_{3 \times 6} & \Phi_\alpha^{(j)} \end{bmatrix} \quad (11)$$

Regarding the COM-to-PCO consider parameters $\Delta \vec{p}_c, \Delta \vec{p}_d$, these are left expressed in the body-frame. Hence their STM is identity *i.e.* static in the body frame. Else, if expressed in a non-body frame, their STM must reflect the time-varying rotation from the body to the frame of relevance. Next, the measurement update steps are presented. Given an observed measurement \vec{z}_t of size m , the innovation, or prefit residual, $\vec{v}_t \in \mathbb{R}^m$ is

$$\vec{v}_t = \vec{z}_t - h(\vec{x}_{t|t-1}, \vec{w}_{t|t-1}, \mathbf{q}(t)) \quad (12)$$

where $\vec{x}_{t|t-1} \in \mathbb{R}^n$, $\vec{w}_{t|t-1} \in \mathbb{R}^\ell$, and $h : \mathbb{R}^{n+\ell} \times \mathbb{H} \rightarrow \mathbb{R}^m$ is the non-linear measurement model; then $\mathbf{H}_t^{(x)} \in \mathbb{R}^{m \times n}$ and $\mathbf{H}_t^{(w)} \in \mathbb{R}^{m \times \ell}$ are the first-order measurement sensitivities with respect to states \vec{x} and consider parameters \vec{w} ; $\mathbf{R}_t \in \mathbb{R}^{m \times m}$ is the modeled measurement covariance at t , positive definite at construction. A review of GRAPHIC and SDCP models can be found in the references [1, 21, 39, 50]. The innovation covariance, with consider parameters \vec{w} included, is expressed as

$$\mathbf{V}_t = \underbrace{\mathbf{H}_t^{(x)} \Sigma_{t|t-1}^{(x)} \mathbf{H}_t^{(x)\top}}_{\text{positive definite form}} + \underbrace{\mathbf{H}_t^{(x)} \Sigma_{t|t-1}^{(xw)} \mathbf{H}_t^{(w)\top} + \mathbf{H}_t^{(w)} \Sigma_{t|t-1}^{(wx)} \mathbf{H}_t^{(x)\top}}_{\text{not guaranteed positive definite numerically}} + \underbrace{\mathbf{H}_t^{(w)} \Sigma_{t|t-1}^{(w)} \mathbf{H}_t^{(w)\top}}_{\text{positive definite form}} + \mathbf{R}_t \quad (13)$$

where it must be noted that in Equation 13, the sum of two matrices that are transposes of each other will result in symmetric but not necessarily PD. Ideally, \mathbf{V}_t should always be PD if factorized in block form. However, in practice, numerical errors from finite precision and rounding accumulations can compound. Hence, the innovation covariance \mathbf{V}_t for the conventional CEKF is might not guarantee PD. Since the optimal Kalman gain \mathbf{K}_t scales inversely with the uncertainty of the innovation, a catastrophic singularity may occur mid-flight if the inverse of \mathbf{V}_t does not exist. In light of this, regularizing the innovation with an extra term $\bar{\mathbf{V}}$ is proposed in Equation 14, in order to numerically guarantee the existence of the inverse in Equation 14 during actual computations.

$$\mathbf{K}_t = \left(\boldsymbol{\Sigma}_{t|t-1}^{(x)} \mathbf{H}_t^{(x)\top} + \boldsymbol{\Sigma}_{t|t-1}^{(xw)} \mathbf{H}_t^{(w)\top} \right) \left(\mathbf{V}_t + \bar{\mathbf{V}} \right)^{-1} \quad (14)$$

The term $\bar{\mathbf{V}}$ is added to possibly non-PD terms such that $\mathbf{V}_t + \bar{\mathbf{V}}$ is PD and hence invertible. The construction of $\bar{\mathbf{V}}$ that makes the smallest possible adjustment to the terms within the inverse in Equation 14, as measured by the trace, can be found as follows. First, the sum of matrices that is non-guaranteed PD is real and symmetric and hence diagonalizable,

$$\boldsymbol{\Psi} \boldsymbol{\Lambda} \boldsymbol{\Psi}^\top = \text{eig} \left(\mathbf{H}_t^{(x)} \boldsymbol{\Sigma}_{t|t-1}^{(xw)} \mathbf{H}_t^{(w)\top} + \mathbf{H}_t^{(w)} \boldsymbol{\Sigma}_{t|t-1}^{(wx)} \mathbf{H}_t^{(x)\top} \right) \quad (15)$$

Then, for diagonal indices $i \in [1, m]$ along $\boldsymbol{\Lambda}$, where m is the number of measurements, if a negatively valued λ_i is found, the corresponding value of γ_i is set to $-\lambda_i$; otherwise, it is set to zero since the eigenvalues are already positive,

$$\bar{\mathbf{V}} = \boldsymbol{\Psi} \cdot \text{diag}([\gamma_1, \gamma_2, \dots, \gamma_m]) \cdot \boldsymbol{\Psi}^\top \quad \text{where } \gamma_i = \max(0, -\lambda_i) \text{ and } \lambda_i \text{ are diagonals of } \boldsymbol{\Lambda} \quad (16)$$

thereby ensuring that $\boldsymbol{\Psi} \boldsymbol{\Lambda} \boldsymbol{\Psi}^\top + \bar{\mathbf{V}}$ will have only non-negative eigenvalues. In practice, eigen-decomposition at each measurement update is costly for flight. Independent measurements per transmitter is often assumed in GNSS [39]. This allows measurements to be processed sequentially as scalars ($m = 1$). Hence, $\bar{\mathbf{V}} \in \mathbb{R}$, and Equation 16 simplifies to:

$$\bar{\mathbf{V}} = \max \left(0, - \left(\mathbf{H}_t^{(x)} \boldsymbol{\Sigma}_{t|t-1}^{(xw)} \mathbf{H}_t^{(w)\top} + \mathbf{H}_t^{(w)} \boldsymbol{\Sigma}_{t|t-1}^{(wx)} \mathbf{H}_t^{(x)\top} \right) \right) \quad (\text{scalar}) \quad (17)$$

The measurement update of the *a posteriori* state mean applies the sub-optimal Kalman gain,

$$\vec{x}_{t|t} = \vec{x}_{t|t-1} + \mathbf{K}_t \vec{v}_t \quad (18)$$

Then, the Joseph form measurement update guarantees the *a posteriori* state covariance in Equation 20 is PD,

$$\mathbf{U}_t = \left[[\mathbf{K}_t \mathbf{H}_t^{(x)} - \mathbf{I}_{n \times n}], [\mathbf{K}_t \mathbf{H}_t^{(w)}] \right] \quad (19)$$

$$\boldsymbol{\Sigma}_{t|t}^{(x)} = \mathbf{U}_t \boldsymbol{\Sigma}_{t|t-1} \mathbf{U}_t^\top + \mathbf{K}_t \mathbf{R}_t \mathbf{K}_t^\top \quad (\text{preserves positive definiteness}) \quad (20)$$

$$\boldsymbol{\Sigma}_{t|t}^{(xw)} = (\mathbf{I}_{n \times n} - \mathbf{K}_t \mathbf{H}_t^{(x)}) \boldsymbol{\Sigma}_{t|t-1}^{(xw)} - \mathbf{K}_t \mathbf{H}_t^{(w)} \boldsymbol{\Sigma}_{t|t-1}^{(wx)} \quad (21)$$

For brevity, the full derivation of the CEKF Joseph form, as well as an analysis of its stability and runtimes, is published as an internal note [51]. No optimality conditions are imposed on \mathbf{K}_t . An important trade-off is that in the Joseph form, most terms are dense, and hence sparse matrix operations cannot be fully exploited for speed, in exchange for numerical stability.

C. Process Noise Modeling

To achieve required orbit prediction accuracies, including during data gaps, the process noise model \mathbf{Q}_t must capture orbit propagation uncertainties and unmodeled dynamics while preserving state correlation structures [45, 54, 55]. When the spectral noise density accurately reflects these correlations, the resulting process noise preserves them appropriately. An exponential spatial correlation model is adopted to capture inter-spacecraft dynamics coupling,

$$\beta_{ij} = \exp(-d_{ij}/D_0) \quad (22)$$

which encodes correlations between spacecraft i and j as a function of their separation d_{ij} , where D_0 is a tunable correlation length scale. This model is a spatial analog to the first-order Gauss-Markov process in time [56]. It intuitively that the dynamics of nearby spacecraft are more strongly correlated than those farther apart. Let $\sigma_R, \sigma_T, \sigma_N$ be the scalar components of the dynamics spectral noise density, decoupled along each axis of the RTN frame. Consequently, the spectral noise density matrices for individual and joint spacecraft dynamics, \mathbf{S}_α and $\mathbf{S}_\alpha^{(ij)}$, are defined as

$$\mathbf{S}_\alpha^{(ij)} \equiv \begin{bmatrix} \mathbf{S}_\alpha & \beta_{ij} \mathbf{S}_\alpha \\ \beta_{ij} \mathbf{S}_\alpha & \mathbf{S}_\alpha \end{bmatrix}, \text{ where } \mathbf{S}_\alpha \equiv \text{diag} \left(\begin{bmatrix} \sigma_R & \sigma_T & \sigma_N \end{bmatrix} \right) \quad (23)$$

and both \mathbf{S}_α and D_0 are user-defined. The joint process noise covariance for the Cartesian states of spacecraft i and j , denoted $\mathbf{Q}_{rv\alpha}$, is analytically derived by mapping the spectral noise density onto the Cartesian states via the process noise mapping matrix $\boldsymbol{\Gamma}$, and propagating it through the Cartesian state transition matrix $\boldsymbol{\Phi}_{rv\alpha}(t, \tau)$ [57], as

shown in Equation 24. If the STM is integrable and across a short time interval Δt , Equation 24 can be approximated in Equation 25,

$$\mathbf{Q}_{rv\alpha} = \int_{t_0}^{t_0+\Delta t} \Phi_{rv\alpha}(t_0, \tau) \cdot \Gamma(\tau - t_0) \cdot \mathbf{S}_\alpha^{(ij)} \cdot \Gamma(\tau - t_0)^\top \cdot \Phi_{rv\alpha}(t_0, \tau)^\top d\tau \quad (24)$$

$$\approx \Phi_{rv\alpha}(t_0, t_0 + \Delta t) \cdot \Gamma(\Delta t) \cdot \mathbf{S}_\alpha^{(ij)} \cdot \Gamma(\Delta t)^\top \cdot \Phi_{rv\alpha}(t_0, t_0 + \Delta t)^\top \quad (25)$$

The joint-spacecraft process noise mapping matrix Γ for spacecraft i and j over a time interval Δt is simply

$$\Gamma(\Delta t) = \begin{bmatrix} \mathbf{C}^{(i)} \tilde{\Gamma}(\Delta t) & \mathbf{0}_{9 \times 3} \\ \mathbf{0}_{9 \times 3} & \mathbf{C}^{(j)} \tilde{\Gamma}(\Delta t) \end{bmatrix}, \quad \text{where} \quad \tilde{\Gamma}(\Delta t) = \begin{bmatrix} \frac{1}{2} \Delta t^2 \cdot \mathbf{I}_{3 \times 3} \\ \Delta t \cdot \mathbf{I}_{3 \times 3} \\ (1 - \theta^2) \cdot \mathbf{I}_{3 \times 3} \end{bmatrix} \quad (26)$$

where $\theta = e^{-\Delta t / \tau_{ae}}$ is the time-decay of the empirical accelerations, and $\mathbf{C}^{(i)}, \mathbf{C}^{(j)}$ ensure that coordinate frames are handled correctly. In the two-spacecraft state vector of Equation 3, positions and velocities are in Earth-Centered Inertial (ECI), while empirical accelerations are in RTN. Let the RTN-to-ECI rotation be $\begin{bmatrix} ECI \mathbf{R}_{RTN}^{(i)} \end{bmatrix} \in \mathbb{R}^{3 \times 3}$, and let $[\omega^\times]$ be the angular velocity of RTN with respect to ECI, in skew-symmetric form, in the RTN basis. Then, the coordinate frame mapping for spacecraft i is

$$\mathbf{C}^{(i)} = \begin{bmatrix} \begin{bmatrix} ECI \mathbf{R}_{RTN}^{(i)} \end{bmatrix} & \mathbf{0}_{3 \times 3} & \mathbf{0}_{3 \times 3} \\ \begin{bmatrix} ECI \mathbf{R}_{RTN}^{(i)} \end{bmatrix} [\omega^\times] & \begin{bmatrix} ECI \mathbf{R}_{RTN}^{(i)} \end{bmatrix} & \mathbf{0}_{3 \times 3} \\ \mathbf{0}_{3 \times 3} & \mathbf{0}_{3 \times 3} & \mathbf{I}_{3 \times 3} \end{bmatrix} \quad (27)$$

The analytical process noise can now be evaluated by substituting 27 into 26, and then 23, 11, 26 into 25. The result is:

$$\mathbf{Q}_{rv\alpha} = \begin{bmatrix} \mathbf{Q}_{rv\alpha}^{(i)} & \mathbf{Q}_{rv\alpha}^{(ij)} \\ \mathbf{Q}_{rv\alpha}^{(ji)} & \mathbf{Q}_{rv\alpha}^{(j)} \end{bmatrix} \quad (28)$$

$$\begin{aligned} \mathbf{Q}_{rv\alpha}^{(i)} &= \Phi_{rv\alpha}^{(i)} \cdot \mathbf{C}^{(i)} \cdot \tilde{\Gamma}(\Delta t) \cdot \mathbf{S}_\alpha \cdot \tilde{\Gamma}(\Delta t)^\top \cdot \mathbf{C}^{(i)\top} \cdot \Phi_{rv\alpha}^{(i)\top} \\ \text{where} \quad \mathbf{Q}_{rv\alpha}^{(j)} &= \Phi_{rv\alpha}^{(j)} \cdot \mathbf{C}^{(j)} \cdot \tilde{\Gamma}(\Delta t) \cdot \mathbf{S}_\alpha \cdot \tilde{\Gamma}(\Delta t)^\top \cdot \mathbf{C}^{(j)\top} \cdot \Phi_{rv\alpha}^{(j)\top} \\ \mathbf{Q}_{rv\alpha}^{(ij)} &= \mathbf{Q}_{rv\alpha}^{(ji)\top} = \Phi_{rv\alpha}^{(i)} \cdot \mathbf{C}^{(i)} \cdot \tilde{\Gamma}(\Delta t) \cdot (\beta_{ij} \mathbf{S}_\alpha) \cdot \tilde{\Gamma}(\Delta t)^\top \cdot \mathbf{C}^{(j)\top} \cdot \Phi_{rv\alpha}^{(j)\top} \end{aligned} \quad (29)$$

The full process noise matrix for the two-spacecraft state vector of Equation 3, including receiver clock biases tracked for k GNSS constellations, and c channels each for ZDCP and SDCP float ambiguities, has the following structure:

$$\mathbf{Q}_t = \begin{bmatrix} \mathbf{Q}_{rv\alpha}^{(i)} & \mathbf{0}_{9 \times k} & \mathbf{Q}_{rv\alpha}^{(ij)} & \mathbf{0}_{9 \times k} & \mathbf{0}_{9 \times c} & \mathbf{0}_{9 \times c} \\ \mathbf{0}_{k \times 9} & \mathbf{Q}_{c\delta t}^{(i)} & \mathbf{0}_{k \times 9} & \mathbf{0}_{k \times k} & \mathbf{0}_{k \times c} & \mathbf{0}_{k \times c} \\ \mathbf{Q}_{rv\alpha}^{(ji)} & \mathbf{0}_{9 \times k} & \mathbf{Q}_{rv\alpha}^{(j)} & \mathbf{0}_{9 \times k} & \mathbf{0}_{9 \times c} & \mathbf{0}_{9 \times c} \\ \mathbf{0}_{k \times 9} & \mathbf{0}_{k \times k} & \mathbf{0}_{k \times 9} & \mathbf{Q}_{c\delta t}^{(j)} & \mathbf{0}_{k \times c} & \mathbf{0}_{k \times c} \\ \mathbf{0}_{c \times 9} & \mathbf{0}_{c \times k} & \mathbf{0}_{c \times 9} & \mathbf{0}_{c \times k} & \mathbf{Q}_{N_{ZD}} & \mathbf{0}_{c \times c} \\ \mathbf{0}_{c \times 9} & \mathbf{0}_{c \times k} & \mathbf{0}_{c \times 9} & \mathbf{0}_{c \times k} & \mathbf{0}_{c \times c} & \mathbf{Q}_{N_{SD}} \end{bmatrix} \quad (30)$$

This analytical process noise model provides a physically grounded approach aligned with the filter's estimate of the required dynamic noise compensation, while preserving the correlation structure between the Cartesian states. It also mitigates manual tuning of process noise parameters. Substantial improvements in state prediction accuracy during data gaps, as compared to the manually-tuned diagonal process noise of [20], will be demonstrated in Section VI.

D. Measurement Noise Modeling

Measurement noise modeling \mathbf{R}_t is critical in deciding how the filter weighs the uncertainty of observations against predicted states. Since correlated measurement biases are already canceled in the GRAPHIC and SDCP measurements, while remaining biases are actively estimated in the state, the filter is primarily concerned with modeling the thermal noise. This section outlines the process of thermal noise modeling, using a Novatel OEM628 GNSS receiver, and an ANTCOM 1.9G1215P antenna. Both units are near-identical representations of the flight units onboard the VISORS spacecraft, with flight heritage. The antenna gain pattern is made available to the flight software via a parametric fit of the actual calibrated data, as seen in Figure 6. Antenna gain values can be sampled from this parametric fit based on the elevation-azimuth. With the gain values, the Carrier-to-Noise Ratio C_{N_0} can then be computed through a link budget for various elevation angles in Table 7,

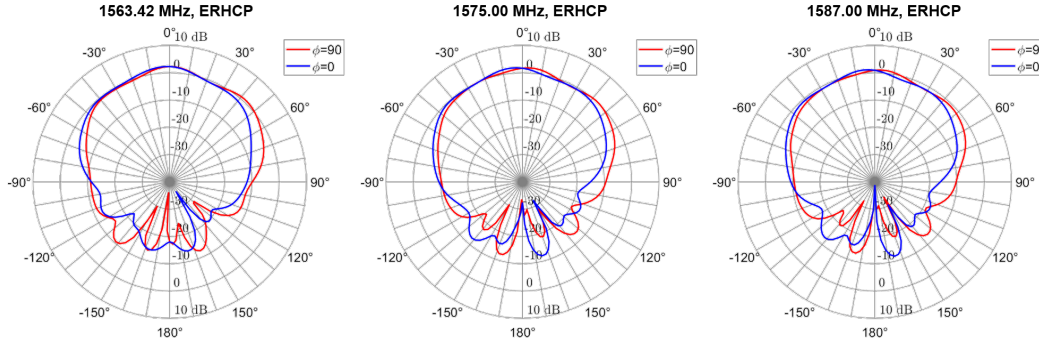


Fig. 6 Calibrated antenna gain of the 1.9G1215P-12S-2-OSR model with orientation ϕ (Credits: ANTCOM)

Table 7 Link budget analysis and thermal noise tabulation for the Novatel OEM628 and an ANTCOM 1.9G1215P antenna, at GPS L1 $f = 1575.42$ MHz. Elevation is measured from the antenna plane. Free space path loss assumes a fixed slant range of 20,000km. Carrier signal strength (C) [dBW] is the sum of gains and losses from the antenna, receiver, GPS transmitter, and the free space path.

		Zenith	Roll-Off	Horizon	Nadir
Elevation	(\cdot) $^\circ$	90	60	0	-90
Antenna Gain	dBW	1.7	-0.6	-10.9	-15.0
Receiver LNA Gain	dBW	30.0			
Receiver Circuit and Polarization Loss	dBW	-4.0			
GPS Antenna Gain	dBW	13.5			
GPS Transmit Power	dBW	14.25			
GPS Transmit Loss	dBW	-1.25			
Free Space Path Loss	dBW	-182.419			
Atmospheric Losses	dBW	-0.10			
Noise Spectral Density (N_0)	dBW/Hz	-169.919			
Carrier Signal Strength (C)	dBW	-125.3185	-127.6185	-137.9185	-142.0185
Carrier-to-Noise Ratio (C_{N_0})	dBW \cdot Hz	41.7	39.4	29.1	25.0
Pseudorange Thermal Noise σ_ρ	m	0.149	0.194	0.634	1.016
Carrier Phase Thermal Noise σ_ϕ	mm	0.682	0.887	2.909	4.664

The signal-to-noise ratio S_{NR} relates to C_{N_0} [dB-Hz] via a log-to-linear scale conversion $S_{NR} = 10^{C_{N_0}/10}$. An analytical thermal noise model formulated by Psiaki and Mohiuddin [41] for undifferenced carrier phase σ_ϕ in Equation 31 and raw pseudorange σ_ρ in Equation 32 is referenced below for convenience,

$$\sigma_\phi = \frac{\lambda}{2\pi} \sqrt{\frac{B_{PLL}}{2S_{NR}}} \quad [\text{meters}] \quad (31)$$

$$\sigma_\rho = ct_c \sqrt{\frac{B_{DLL} t_{eml}}{2t_c S_{NR}} \left(1 + \frac{1}{t_{acc} S_{NR}}\right)} \quad [\text{meters}] \quad (32)$$

where B_{PLL} and B_{DLL} are the receiver loop bandwidths for the receiver Phase-Lock Loop (PLL) and Delay-Lock Loop (DLL) respectively; t_{eml} denotes the early-minus-late correlator spacing in seconds; t_{acc} refers to the pre-detection integration time over which signal energy is accumulated before discriminator evaluation; $t_c = 1/f_c$ is the chipping

period of the pseudorandom code, where $f_c = 1.023$ MHz for GPS L1 C/A; c and λ are the speed of light and wavelength. Typically, B_{PLL} and B_{DLL} may be disclosed by the manufacturer, but often, very specific design parameters such as t_{eml} and t_{acc} may not be. In the case of the Novatel OEM628, $B_{DLL} = 0.0076$ Hz and $B_{PLL} = 15$ Hz. It is assumed that $t_{eml} = 1$ -chip period, which is reasonable for modern receivers, and that the accumulation interval t_{acc} is sufficiently long so that $t_{acc} S_{NR} \gg 1$. This simplifies the pseudorange thermal noise model to Equation 33,

$$\sigma_\rho \approx \frac{c}{f_c} \sqrt{\frac{B_{DLL}}{2S_{NR}}} \quad [\text{meters}] \quad (33)$$

The filter may then discern thermal noise 31 and 33 using a look-up table of the antenna gain values, which are in turn based on the azimuth-elevation of the arriving signal.

E. Integer Ambiguity Resolution

The topic of IAR is well-researched in literature. Hence, the IAR module, based on the Modified LAMBDA algorithm [2, 58] is only briefly outlined in Figure 7, for the completion of the full presentation.

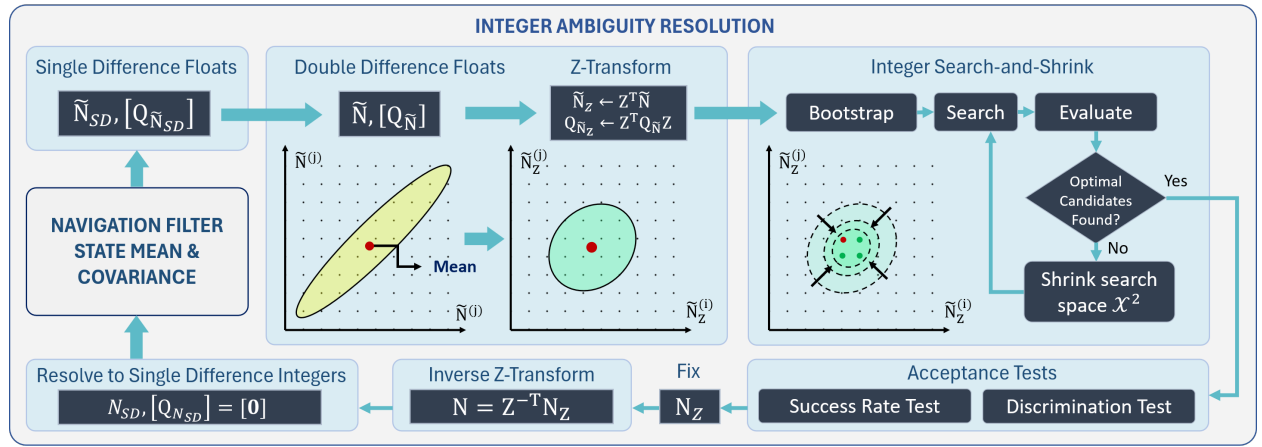


Fig. 7 Block diagram of the Integer Ambiguity Resolution (IAR) block, expanded from Figure 5.

First, SDCP floats \tilde{N}_{SD} are double-differenced to DDCP floats \tilde{N} . Components of the \tilde{N} vector are highly correlated due to the common SDCP reference measurement. Decorrelation using the integer-preserving Z-transform [2] reduces the size of the search space prior to integer search. The Z-transform matrix \mathbf{Z} is an integer approximation of the lower triangular matrix \mathbf{L} , which comes from the $\mathbf{Q}_{\tilde{N}} = \mathbf{L}\mathbf{D}\mathbf{L}^T$ decomposition. \mathbf{Z} is derived by imposing the integer constraints given in [59], so that

$$\mathbf{Q}_{\tilde{N}_z} = \mathbf{Z}^T \mathbf{L} \mathbf{D} \mathbf{L}^T \mathbf{Z} \approx \mathbf{D} \quad (34)$$

The Z-transformed DDCP float ambiguities $\tilde{N}_z = \mathbf{Z}^T \tilde{N}$. The result is a transformed mean \tilde{N}_z and covariance $\mathbf{Q}_{\tilde{N}_z}$ that is almost decorrelated, though not completely due to the integer constraints. The initial guess of integer candidates is done via recursive conditional rounding [60]. The rounded integers allow bounding of the initial search width in the discrete integer space, which is successively shrunk during integer search to minimize the computational costs of evaluating sub-optimal candidates. For each integer candidate N_z , the integer least squares objective function to minimize over all candidates is

$$\min_{N_z} ||N_z - \tilde{N}_z||_{\mathbf{Q}_{\tilde{N}_z}^{-1}}^2 \quad (35)$$

When the best candidate can no longer be improved, it is only resolved into an integer if it passes recommended acceptance tests, such as the Success Rate and Discrimination Tests [60], or meets an Ambiguity Dilution of Precision (ADOP) [61] threshold. This paper adopts the Success Rate Test with a 99% threshold and the Discrimination Test.

IV. Navigation Fault Detection, Isolation, and Recovery

The Fault Detection, Isolation, and Recovery (FDIR) module is designed to ensure continuous and robust navigation against anomalous measurements. Three key sub-functions of FDIR are highlighted in red in the architecture of Figure 8,

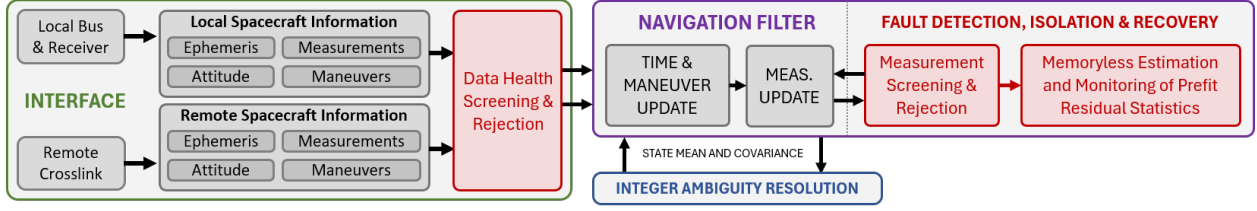


Fig. 8 Architecture of the Fault Detection Isolation and Recovery (FDIR) block, expanded from Figure 5.

A. Data Health Screening and Rejection

The health of incoming measurements, maneuvers, attitudes, ephemerides, and telecommands are screened for validity. Packet headers and checksums are inspected. Sanity checks are conducted *e.g.* unexpectedly low or high pseudorange, carrier phase, C/N_0 values etc; bad GNSS ephemeris values; time-relevance of maneuvers or measurements in-the-past etc. This includes local (bus) and remote (through crosslink) data. These first-layer checks ensure data integrity down the signal chain in subsequent modules, thereby satisfying Requirement R2.3. Potential numerical instabilities are checked, and exceptions are raised if any, as per Requirement R2.8. Cycle slip flags from the receiver, if any, are checked too, as per Requirement R2.9.

B. Measurement Screening and Rejection

Measurement outliers are identified by comparing prefit residuals with κ multiples of the trace of the innovation variance Equation 13, where κ is a configurable parameter *e.g.* $\kappa = 5$, and \mathbb{I} is simply an indicator function,

$$\mathbb{I} \left(\|\tilde{\mathbf{v}}\|_2^2 > \kappa \cdot \text{tr}(\mathbf{V}) \right) = \begin{cases} \text{Accept if } \text{True}, \\ \text{Discard if } \text{False}, \end{cases} \quad (36)$$

The innovation covariance from 13 provides an adaptive threshold that accurately reflects the immediate prefit uncertainty, as it sums contributions from both modeled measurement noise plus current state uncertainties projected onto the measurement subspace. Adaptive thresholds more accurately reflects the underlying uncertainty of prefit residuals, and contrasts with fixed gated thresholds that must be manually tuned based on domain knowledge [20, 21]. However, careful initialization of the *a priori* state covariance and accurate measurement uncertainty modeling are needed. Overconfident initialization may cause rejection of valid measurements as $\kappa \cdot \text{tr}(\mathbf{V})$ provides overly tight bounds, while underconfident initialization may admit outliers.

C. Memoryless Estimation and Monitoring of Prefit Residual Statistics

While the innovation covariance provides a snapshot of prefit residual uncertainty, a moving-window estimator could capture time-varying statistics. Algorithm 1 provides a memoryless and statistical approach to fault detection,

Algorithm 1 Memoryless Estimation and Monitoring of Prefit Residual Statistics

```

1: for each computed prefit residual  $r$  do
2:    $\mu_{k+1} \leftarrow (1 - \rho)\mu_k + \rho \cdot r$                                  $\triangleright$  Fading memory update of estimated mean of prefit residuals
3:    $\sigma_{k+1}^2 \leftarrow (1 - \rho)\sigma_k^2 + \rho \cdot (r - \mu_k)$                  $\triangleright$  Fading memory update of estimated sigma of prefit residuals
4:    $S_{k+1} \leftarrow (1 - \rho)S_k$                                         $\triangleright$  Decay the score of the number of outliers
5:   if  $\|r - \mu_{k+1}\|^2 > \eta \cdot \sigma_k^2$  then
6:      $S_{k+1} \leftarrow S_{k+1} + 1$                                         $\triangleright$  If prefit residual  $r$  lies outside  $\eta \cdot \sigma_k^2$  bounds, increase outlier count by +1
7:   end if
8: end for
9: if  $\left(1 - \frac{S_{k+1}}{M}\right) > g(\mu_{k+1}, \sigma_{k+1}^2)$  then
10:  do emit navigation incapability flag  $\triangleright$  Flag incapable if number of outliers violate concentration inequalities
11: end if

```

where M is the ‘moving window’ size; $\rho \equiv 1/M$ is the forget-factor; μ_k and σ_k^2 are the empirically estimated sample mean and covariance of the prefit residuals at time k ; S_k is a fading count of outliers residing beyond the tail bounds of $\eta\sigma_k^2$ at time k ; η is a hyper-parameter; and $g(\mu_i, \sigma_i^2)$ returns a concentration inequality upper bound for the outlier fraction outside the $\eta\sigma_k^2$ tails.

The core idea of Algorithm 1 is to model prefit residuals as a stationary stochastic process with non-zero decay, implying a time-invariant mean and variance [56]. These are estimated empirically using a memoryless moving window. If enough anomalous measurements occur such that the estimated outlier fraction exceeds $g(\mu_i, \sigma_i^2)$, the algorithm deems the current distribution invalid and raises an incapability flag. For general distributions, g may use Chebyshev’s Inequality [56]; for unimodal ones, the Vysochanskij-Petunin inequality applies [62, 63]. Importantly, the moving window does not retain time-series history of M samples, making its memoryless design well suited for flight computers. Figure 9 gives the reader a preview ahead of the results, to the FDIR flight software response to and recovery from a deliberately injected cycle slip.

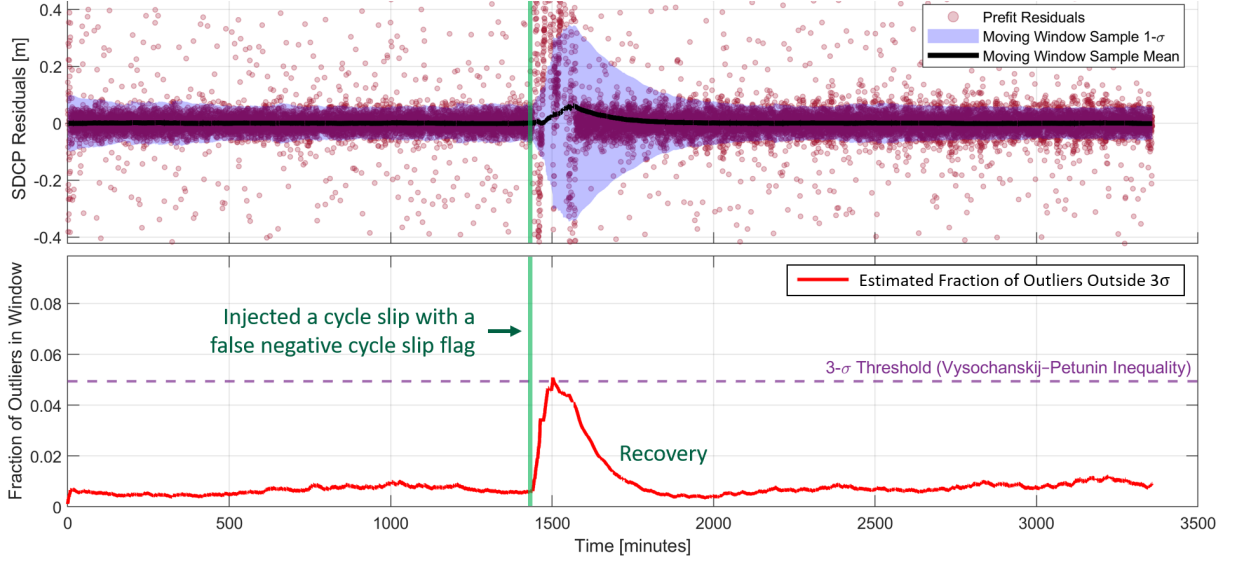


Fig. 9 Plot of moving-window sample mean and variance of SDCP measurement prefit residuals (top) and moving-window estimate of number of outliers outside $\eta\sigma^2$ (bottom) for $\eta = 3$ and $M = 6000$; cycle slips were injected at $t = 24$ hours for GPS vehicles currently tracked in 6/12 active channels of one spacecraft. The software detected a fault once outlier counts violated the Vysochanskij-Petunin inequality. The filter auto-recovered after 1 orbit. Default recovery action re-initializes the mean and covariances of float ambiguities.

Figure 9 shows a time-series of SDCP measurement prefit residuals, with cycle slips injected at $t = 24$ hours, from a two-spacecraft campaign initialized with a 200m along-track separation over ≈ 2.5 days. Measurements are received every 10s. Each slip was modeled as a Gaussian with bias and noise $\approx 1500 \pm 150$ cycles. Two observations followed: (1) most measurements were rejected by Equation 36, and (2) accepted measurements had large enough residuals to bump up the outlier count until it exceeded g , triggering an anomaly flag. The system responded by resetting the mean and covariance of \tilde{N}_{ZD} and \tilde{N}_{SD} to their *a priori* distributions. Post-reset, the prefit residuals returned to normal values after 1 orbit, with gradual recovery in the outlier score. This exhibits robust navigation and successful FDIR by leveraging statistical guarantees in a memoryless algorithm suited for flight use.

V. Navigation Software Design

A. Overview of Software Design and Interface

The `Navigation` class executes timely, accurate, and robust state estimation by fusing local and remote (crosslink) measurements with auxiliary data (e.g., maneuvers, attitude, ephemerides). A decision logic determines whether each incoming measurement triggers a filter update. On events e.g. state estimates, crosslink, telemetry etc, `Navigation` calls back to a `NavigationDelegate` inherited by the host class. The software emphasizes encapsulation, modularity, robustness, and efficiency. It is designed for turn-key integration into any host software (referred to here as the `Host`), without additional dependencies. The `Host` communicates via a single header interface, shown in Figure 10. While

written in C++17, the architecture generalizes to any object-oriented language. Best practices are followed to ensure development efficiency, ease of testing, and fast runtimes.

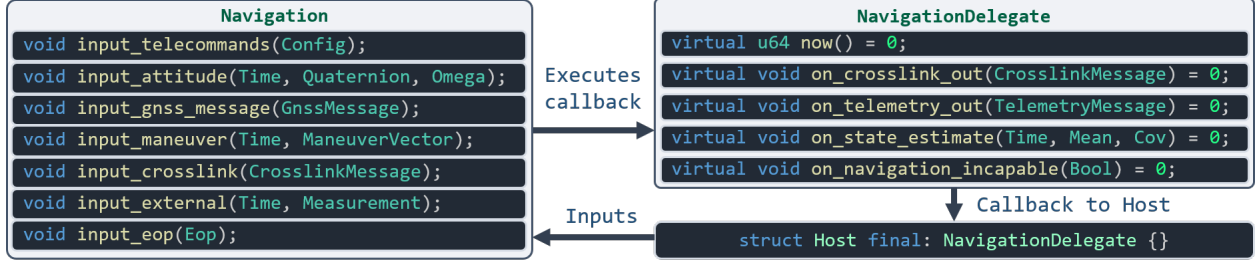


Fig. 10 Software interface reflecting the implementation of Figure 2. Function signatures use C++ style syntax for illustration.

Encapsulation: Implementation details of **Navigation** are hidden behind a Pointer-to-Implementation design (PImpl) to achieve encapsulation with separation of concerns. This reduces compile-time dependencies, as changes to **Navigation** will not require a re-compilation of the **Host** files, since the interface remains unchanged. This facilitates faster development overall.

Modularity and Flexibility of Response Logic: The callback-based interface in Figure 10 allows the **Host** to interface callbacks from **Navigation** through class inheritance, restricting method overrides solely to the host. Method overriding allows the **Host** to customize its behavior in response to callbacks, allowing for flexible response logic and ease of integration.

Robustness to Race Conditions: Ensuring data integrity of **Navigation** in real-time is critical to its successful operation. Only a single thread is ever employed in **Navigation**. The use of lock guards or mutexes is implemented to ensure that only one thread at a time may interact with **Navigation**, which protects states and data from being executed on by several concurrent operations simultaneously. This preserves state consistency, protects data from corruption, and prevents race conditions or deadlock.

Maximizing Software Efficiency with Sparsity: Sparse matrix operations are used wherever possible to reduce runtime, especially given the quadratic growth of covariance size with state dimension. A useful metric is the sparsity ratio $Sp(\mathbf{A}) = 1 - M_0/mn$ for any matrix $\mathbf{A} \in \mathbb{R}^{n \times m}$, where M_0 denotes the number of zero elements. In the time update, the process noise matrix \mathbf{Q}_t is highly sparse, as empirical accelerations do not affect clock offsets or ambiguity states. During the measurement update, the Jacobians $\mathbf{H}_t^{(x)} = \partial h / \partial \bar{x} \in \mathbb{R}^{m \times n}$ and $\mathbf{H}_t^{(w)} = \partial h / \partial \bar{w} \in \mathbb{R}^{m \times \ell}$ are also sparse, as measurements depend only on a subset of state variables. Dynamic programming techniques are adopted also for reuse of intermediate results in repeated matrix operations, reducing redundant computations and improving memory efficiency.

B. Data Streaming and Sequencing

A challenge observed during software integration is that data updates from sensor and actuator streams into **Navigation** are not guaranteed to arrive with a time-of-arrival that is in the same sequence as their time-stamps. This is because data are generated by several independent hardware sources per spacecraft (see Figure 11), each operating with distinct clocks and communicating over separate signal pathways. Since the recursive navigation filter progresses only forward in time, the **Navigation** interface employs a specialized **Queue** object to manage these incoming disordered data streams. The **Queue** buffers, reorders, and emits the updates in order of time stamps for processing by the filter.

The **Queue** is essentially an object executing a streaming-sorting algorithm subjected to temporal constraints. Unlike batch sorting algorithms, it cannot reorder updates that have already been emitted to the filter, nor can it preemptively sort updates not yet received. This limitation means that if no assumptions are made about the maximum delay of an update entering the queue, it is impossible to perform a perfect streaming sort. For example, if the filter's current time is $t = 0$ and a GNSS measurement update with a time stamp of $t = 2$ arrives, a perfect queue would face a dilemma: it cannot emit the $t = 2$ time-stamped update immediately, as there remains the possibility of receiving an earlier $t = 1$ time-stamped update later due to latency, which would need to be emitted first. This uncertainty underscores the need for a pragmatic balance in queuing strategy. A set of critical parameters in the design of the **Queue** are its buffer periods, which are duration for which updates are held before being forwarded to the filter. Short buffer periods enable faster integration of new information, ensuring the filter's estimate remains timely. Conversely, long buffer periods allow the system to accommodate out-of-order messages streaming in later, reducing the likelihood of discarding latent updates. In the extreme case, a zero-second buffer period would immediately emit any updates as they arrive, and any incoming out-of-order updates will be dropped. The **Queue** makes the following assumptions:

- 1) Packets from the same hardware source will arrive in order with respect to each other.
- 2) Packets from any source on the local spacecraft arrive at most 2 seconds late.
- 3) Packets from any source on the remote spacecraft arrive at most 4 seconds late.

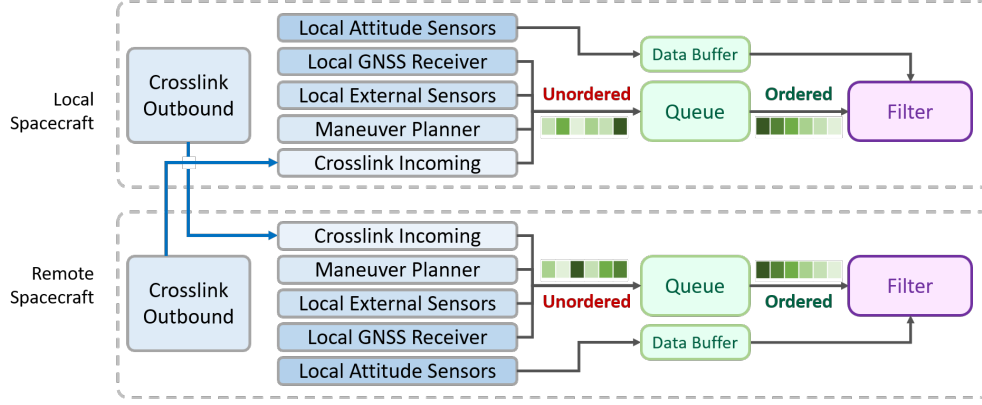


Fig. 11 Queue implemented as a streaming-sorting intermediary between the Interface and the Navigation Filter.

With these assumptions, an ‘optimal’ Queue can be designed, with the understanding that any received updates that violates these assumptions will be dropped. The caveat is that Navigation then requires the ability to schedule (via a callback) any state updates in the future, past the expiration of the buffer period, if data is presently unavailable due to latency. The Queue also intentionally facilitates seamless transitions between absolute and relative state estimation, ensuring robust operation during crosslink outages. If remote updates are unavailable beyond the 4-second buffer, the Queue continues filtering with local data alone and automatically resumes relative navigation once crosslink is restored. This transition mechanism is verified in Section VI to meet Requirement R2.6.

C. Dynamic State Resizing

Onboard compute efficiency is essential for timely, accurate state estimates that support guidance, control, and decision-making downstream. Beyond exploiting sparsity, this work introduces dynamic state resizing to reduce computational load, especially since matrix multiplications scale as $O(n^3)$. Resizing is achievable because not all channels are active. After IAR, fixed integers can be treated as known constants with zero uncertainty. Dynamic resizing removes such inactive states, reducing the state mean and covariance to only active states. Floats are flushed first, integers last, as shown in Figure 12,

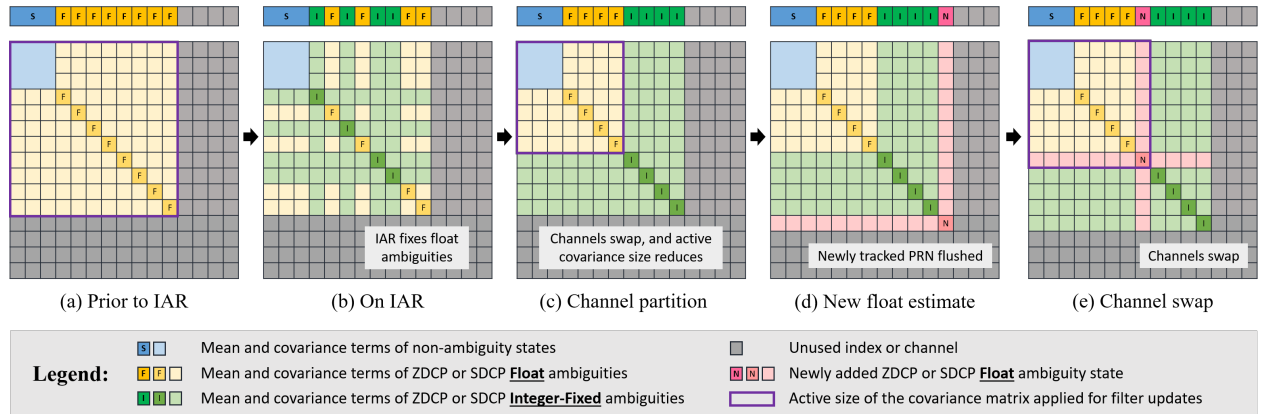


Fig. 12 Dynamic resizing and channel flushing of the active covariance matrix.

In Figure 12, (a) exemplifies the state mean and covariance prior to IAR in which channels may be ZDCP or SDCP float ambiguities; (b) shows the states after successful IAR, which could be performed on any arbitrary channel index; (c) applies channel flushing so that integer-fixed channels are contiguous with unused channels; (d) illustrates the next time instance where a previously untracked float ambiguity from a carrier phase measurement enters the state and occupies

the first unused channel in the state vector; (e) performs a channel swap to flush the new float ambiguities channels with existing ones, in order to ensure that the active states remain contiguous. The final covariance size is hence bounded only by the last float ambiguity channel. Channel flushes can be executed by a series of channel swaps. Channel swaps involve swapping the i -th and j -th indices of the state mean and channel meta-data (PRN ID, GNSS system and signal, lock times etc), followed by swapping the i -th and j -th rows, and then the i -th and j -th columns of the state covariance Σ . This can be represented mathematically using the permutation matrix Π as in $\vec{x} \leftarrow \Pi\vec{x}$ and $\Sigma \leftarrow \Pi\Sigma\Pi^T$.

VI. Test Campaigns and Results

A. Testbed Architecture and Modeling Assumptions

This section describes the end-to-end testbed, referenced to Figure 13, for evaluating the navigation flight software, as well as modeling assumptions in the dynamics, measurements, and simulation environment. The flow of events is scheduled in real-time via a hybrid discrete-time continuous-time event loop [64]. Uncertainty modeling with regards to ground truth dynamics, measurement generation, and spacecraft-specific contributions are summarized in Table 8, Table 9, and Table 10 respectively. The client executes a dynamics-driven event loop in real-time [64], transmitting truth trajectory and attitude at 10-Hz to an IFEN NCS NOVA+ GNSS signal simulator (server). GNSS RF signals then stimulate two Novatel OEM628 GNSS receivers, whose measurements are streamed via serial to two DiGiTaL software instances. Crosslink between each DiGiTaL object is software-emulated with latencies.

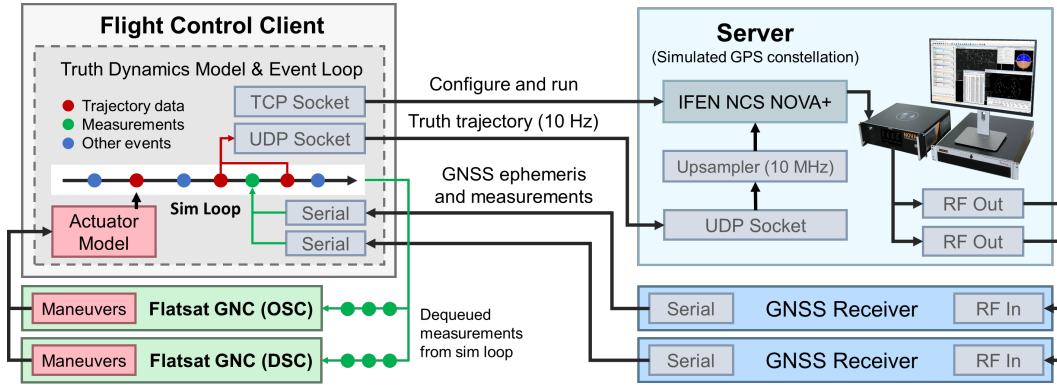


Fig. 13 Hardware-in-the-loop (HIL) testbed for closed-loop evaluation of the DiGiTaL v2 software.

Table 8 Dynamics modeling for both the simulation truth and flight software.

	Ground truth dynamics	Filter dynamics
State representation	Quasi-nonsingular orbital elements	Cartesian
State equations	Gauss' variational equations	Fundamental orbital differential equations
Integrator	RK45 (Dormand-Prince)	RK4 (non-adaptive step size)
Geopotential	GGM05S (60x60)	GGM01S (20x20)
Drag model	NRLMSISE 00, F10.7 = 184.6, $A_p = 18.4$	Harris-Priester
Solar radiation pressure	Analytical sun ephemeris with cylindrical shadow	–
Third body gravity	Analytical Sun & Moon ephemeris	–

Table 9 GNSS signal-in-space conditions modeling

GNSS signals	GPS L1 only, Block IIR-M
GNSS aperture	170 degrees
GNSS gain/phase pattern	Spherical only
GNSS ephemeris source	Broadcast (no corrections)
Ionospheric model	Klobuchar (delay only)
Receiver Earth horizon mask	-20 degrees from horizon
Receiver aperture mask	190 degrees
Receiver simulated LNA	33 dBW
Receiver gain/phase pattern	ANTCOM 1.9G1215A

Table 10 Spacecraft uncertainty parameters.

Parameter	Unit	Dist.	Value
Spacecraft mass	kg	Gaussian	0.04
Spacecraft COM	mm	Uniform	3
GNSS antenna PCO bias	mm	-	50
GNSS antenna PCO noise	mm	Gaussian	1
GNSS antenna direction	arcsec	Gaussian	30
Attitude knowledge	arcsec	Gaussian	20
Maneuver magnitude	%	Gaussian	5
Maneuver direction	arcsec	Gaussian	60

Table 11 Klobuchar ionospheric model parameters used in ground truth measurement emulation.

α_1	α_2	α_3	α_4	β_1	β_2	β_3	β_4
2.794E-8	-7.451E-9	-1.192E-7	1.788E-7	137200	-98300	65540	-393200

B. Requirements Verification and Compliance Tests

This section outlines compliance test scenarios in Table 12, with graduating fidelity. It provides traceability by mapping surveyed requirements of Table 4 to compliance tests, via the RVM in Table 13. Wide test coverage stresses weak points in the software, revealing where software or navigation logic may fail. This uncovers hidden vulnerabilities, across modes of Figure 1, and ensures the system can handle realistic off-nominal conditions. Test campaigns adopt the VISORS mission concept [10] for the full-campaign. For brevity, only scenarios **T.4.1**, **T.4.7**, and **T.7.2** (highlighted in green) are discussed with detailed time-series results in this paper.

Table 12 Full set of compliance test campaigns.

Test Campaign	Test Scenarios
T.1 - Unit Tests	T.1.1 - Software built-in-tests to verify numerical correctness and function behaviour
T.2 - Initialization and Interfacing	T.2.1 - Receiver cold start test (no prior almanac)
	T.2.2 - Receiver warm start test (with prior almanac)
	T.2.3 - Sample packet test for crosslink, attitude, telecommands and propulsion
T.3 - Software Emulated GNSS in the Loop Nominal Scenarios	T.3.1 - Standby, uncontrolled, 12 hours
	T.3.2 - Full campaign (standby-transfer-operations), 36 orbits
	T.3.3 - Full mission, 10 campaigns with 1 week of Standby between with role switches
T.4 - Software Emulated GNSS in the Loop for Degraded Scenarios	T.4.1 - Standby, uncontrolled, 3 orbits. Total crosslink outage for 1 orbit
	T.4.2 - Intermittent crosslink drop-rate of 1%, with 99% persistence
	T.4.3 - GNSS drop-rate of 1%, with 75% persistence
	T.4.4 - Maneuvers successfully executed but with 100% packet drop-rate to navigation
	T.4.5 - Elevated noise in measurements, dynamics, and maneuvers to 300% nominal noise
	T.4.6 - Float ambiguity resolution only, no IAR
	T.4.7 - Software-emulated cycle slip injection
T.5 - Software Emulated GNSS in the Loop for Contingency Scenarios	T.5.1 - Science/operations mode, but force-interrupted with triggered escape
	T.5.2 - Science/operations mode, but force-interrupted with bus safe mode
T.6 - Software Emulated Sweep Tests	T.6.1 - Full campaign, 36 orbits, with a variable sweep over uncertainty parameters
T.7 - Hardware Emulated Real-Time GNSS in the Loop Nominal Scenarios	T.7.1 - Standby, no station-keeping, sun-pointing attitude, 1 day
	T.7.2 - Full campaign, 36 orbits, in real-time (standby-transfer-operations), with role-switch
T.8 - Hardware Earth-Fixed Live-Sky Antenna Test	T.8.1 - Live-sky daytime navigation test
	T.8.2 - Live-sky night time navigation test

All test scenarios in Table 12 are periodically run throughout development, and were presented in the wider VISORS Flight Software review held in Stanford University, in November 2024. This was paneled by notable reviewers in the space flight community from across multiple universities, aerospace companies, and public science agencies.

T.1: Unit tests form the foundation of software validation, with test coverage on navigation functions, state transformations, dynamics and measurement modeling, time scale conversions, coordinate rotations etc. A Continuous-Integration and Continuous-Delivery (CI/CD) pipeline integrates these tests after every software commit to ensure functional correctness and catch edge cases, bugs, or unreachable states, prior to any integrated tests.

T.2: Interface testing validates the accuracy and resilience of the flight software's interaction with data sources. These tests begin with software-emulated GPS receiver packets, crosslink packets, and telecommands. Fidelity progresses to hardware-emulated packets from a NovAtel OEM628 driven by the IFEN NOVA+ GNSS signal simulator as in Figure 13, and then actual live-sky GNSS packets via rooftop antennas for a zero-baseline test. Live-sky tests validate interfacing with both cold (no prior almanac) and warm starts (with almanac) on the receiver. All interfacing algorithms are tested to ensure correct packet parsing, checksum validation, and reliable operation across all conditions.

T.3 - T.6: Software-in-the-loop GNSS emulation is a critical enabler for rapid development and deployment, due to faster-than-real-time testing. Modeling realism remains consistent with Tables 8, 9, 10 and 11. Furthermore, it permits testing Navigation with other emulated subsystems (e.g., Guidance, Control, Safety) for full mission simulation

of VISORS [10]. This framework allows thorough performance evaluation across performance degraded scenarios (T.4), contingency scenarios such as safe modes or during an escape trajectory (T.5), and robustness to variations in uncertainty parameters via sweep tests (T.6). These campaigns graduates the software readiness ahead of an integrated hardware-in-the-loop testing.

T.7 - T.8: Hardware-in-the-loop (HIL) GNSS testing represents the culmination of the test campaign, validating the full analog-digital signal chain with the DiGiTaL v2 navigation flight software at its core. It exercises all components of the software: interfacing, functionality, and performance, in real-time with latencies, and with other software subsystems *e.g.* Guidance, Controller, and Safety, in closed-loop. GNSS measurements generated by the hardware in Figure 13 rely on ground truth states, which are driven by the event loop [64]. The event loop coordinates the dynamics and the timing asynchronously into a single thread across all threads on each hardware unit (the IFEN NOVA+, the local host running the event loop, and each instance of the `Navigation` software. This achieves mission-representative validation of DiGiTaL v2's navigation performance under realistic and real-time operational conditions.

Table 13 Requirements Verification Matrix (RVM) mapping compliance test in Table 12 items to navigation requirements in Table 4

	R1.1	R1.2	R1.3	R1.4	R1.5	R1.6	R2.1	R2.2	R2.3	R2.4	R2.5	R2.6	R2.7	R2.8	R2.9	R3.1	R3.2	R3.3	R3.4	R3.5	R3.6	R3.7	R3.8
T.1.1																							
T.2.1																							
T.2.2																							
T.2.3																							
T.3.1																							
T.3.2																							
T.3.3																							
T.4.1																							
T.4.2																							
T.4.3																							
T.4.4																							
T.4.5																							
T.4.6																							
T.4.7																							
T.5.1																							
T.5.2																							
T.6.1																							
T.7.1																							
T.7.2																							
T.8.1																							
T.8.2																							

Hardware-in-the-Loop Real-Time Test: Here, results from the full VISORS campaign scenario T.7.2 with GNSS hardware-in-the-loop as per Figure 13 in real-time are presented. VISORS is a distributed telescope mission for high-resolution imaging of the Sun in the extreme ultraviolet spectrum, using two 6U CubeSats flying in formation in a Sun-synchronous low-Earth orbit. An Optics Spacecraft (OSC) carries a photon sieve lens, while signals passing through the lens is focused on a Detector Spacecraft (DSC). Observations happen at a 40m baseline with sub-cm alignment requirements. Elaborated details of the concept of operations, as well as specifics on the other subsystems can be found in references [9, 10]. Relative orbit configurations are in Table 14, with epoch set to 12:00AM, 1 Oct 2024 GPST.

Table 14 Reference orbit and quasi-nonsingular relative orbital elements per mode for test conditions.

Reference orbit		Relative orbit modes		
Element	Sun Sync Parameters	Element	Standby (m)	Science (m)
a (km)	$R_E + 500$	$a\delta a$	0	-2.62
e (-)	0.004	$a\delta\lambda$	0	45.21
i (deg)	97.8	$a\delta e_x$	0	-34.51
Ω (deg)	157.5	$a\delta e_y$	200	4.78
$u(t_0)$ (deg)	0	$a\delta i_x$	0	-18.72
LTAN	10:00AM	$a\delta i_y$	200	2.72

T.7.2 conducts a full test campaign that initializes the DSC and OSC in Standby, transitions to Transfer, and then to Science mode, performing one observation per Science orbit. A Laser Rangefinder (LRF) on the OSC and a Reflector on the DSC enable alignment verification via range measurements. Up to 10 Science orbits, and thus 10 alignment attempts, are executed. Midway, a role-switch is executed to transfer relative orbit control from the one spacecraft to the other, to validate that the `Navigation` software instances on both spacecraft remain uninterrupted and performant.

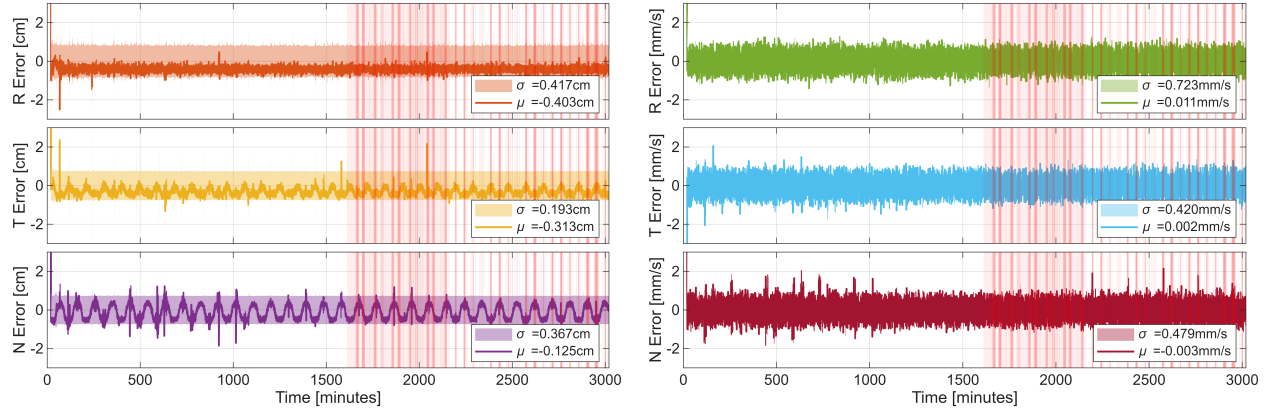
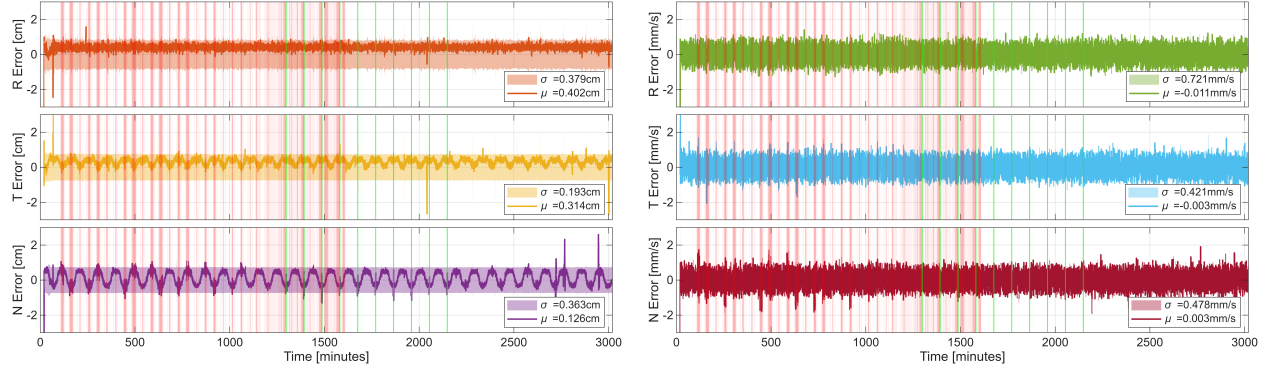
**14a: Relative position error and covariance estimated by DSC****14b: Relative velocity error and covariance estimated by DSC****14c: Relative position error and covariance estimated by OSC****14d: Relative velocity error and covariance estimated by OSC**

Fig. 14 Relative trajectory errors and covariance of a full VISORS campaign (36 orbits). Translucent **red lines** indicate maneuvers, each with impulse bit of $< 2\text{mm/s}$; while **green lines** indicate successful LRF alignment.

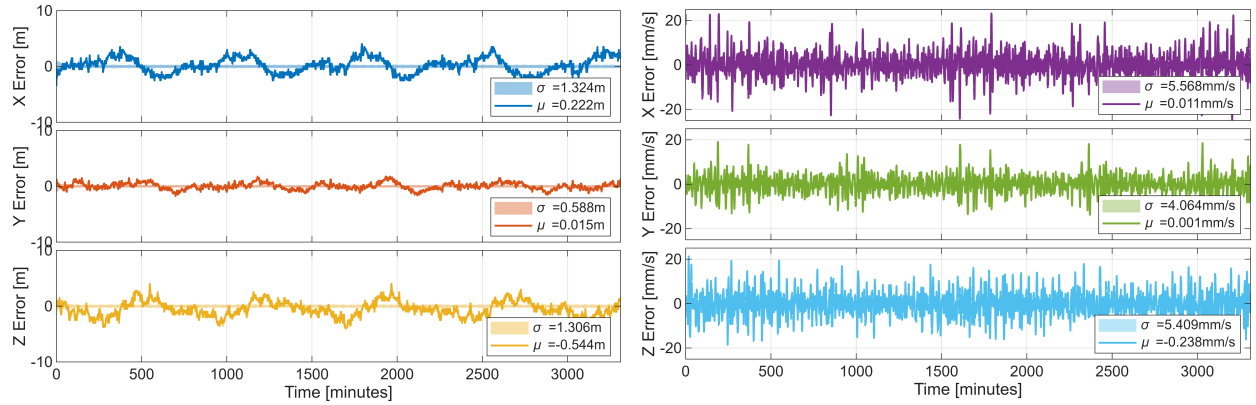
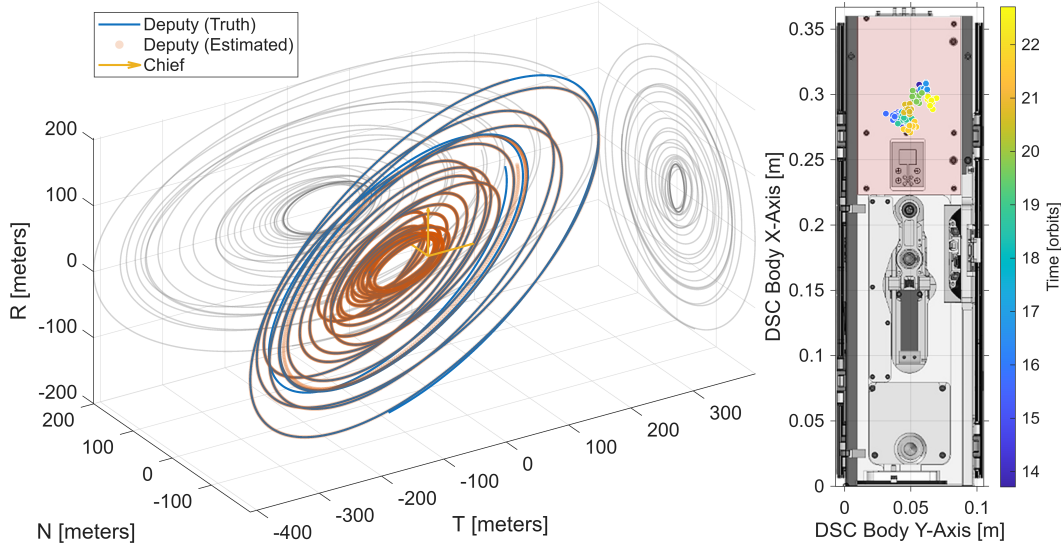
**15a: Absolute ECI position errors of the DSC****15b: Absolute ECI velocity errors of the DSC**

Fig. 15 Absolute ECI state errors of the DSC. OSC results are similar and omitted for brevity.

Out of 10 alignment attempts, 4 met observation requirements. The time of first IAR fix is at $t = 8$ minutes. Oscillations in relative position errors arise due to the presence of unobservable COM-to-PCO variations simulated, according to Table 10. This is despite stress-testing the filter by adopting only a 5mm per-axis magnitude in consider state uncertainty, but applying a 5cm actual bias, as per Table 10 (one order of magnitude larger). Figure 14a and Figure 14c show the filter's covariance envelope converging conservatively around the true error. The relative positive error mean exhibits only a bias of 4mm, 3mm, and 1.25mm in the \hat{R} , \hat{T} , and \hat{N} axes. This desirable result arises, not only due to the presence of consider states, but also because the state vector provides degrees of freedom to absorb static

measurement biases (*e.g.* clock offsets and float ambiguity states). This validates robust state estimation under poorly observed biases. Next, the relative trajectory, LRF scatter grouping, and measurement residuals are presented.



16a: Plot of true and estimated relative orbit, with DSC at the origin. 16b: LRF scatter grouping
Fig. 16 True vs estimated relative trajectory, with LRF scatter on the DSC reflector panel in the body frame.

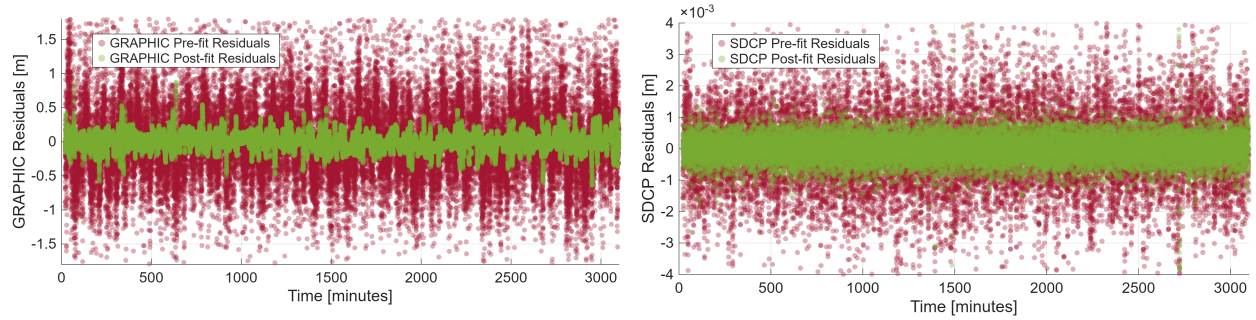


Fig. 17 Pre- and post-fit residuals for GRAPHIC (left) and SDCP (right) for the DSC.

Software-in-the-Loop Simulated Crosslink Outage: Next, scenario T.4.1 is presented. This evaluates the impact of the proposed correlated process noise model on orbit prediction accuracy during crosslink outages. Results from the improved DiGiTaL v2 (Figure 18c and 18d) are compared with the legacy diagonal-only process noise model from DiGiTaL v1 (Figure 18a and 18b) [20]. The formation is initialized as per Table 14, under healthy simulated crosslink for 2 orbits. On the 3rd orbit, a crosslink outage is triggered. As shown in Figure 18, the new correlated process noise model significantly improves relative position and velocity errors during the outage. By accurately preserving the state covariance correlation structure, the filter time update mitigates state error growth from uncompensated dynamics using the correlation between remote and local spacecraft motion – even when remote measurements are lost. This demonstrates that the physically consistent process noise model developed in this work significantly enhances prediction fidelity under degraded navigation. This test scenario also demonstrates seamless transition from relative to absolute-only navigation modes when the crosslink becomes unavailable.

Software-in-the-Loop Simulated Cycle Slip Injection: Next, scenario T.4.7 is presented. Here, since carrier phase ambiguities are software-emulated with control over the true ambiguity values, repeated cycle slips are emulated by corrupting the ground truth ambiguity values once per orbit. This causes sudden prefit residual outliers and large sample variances observed in Figure 19b by the moving-window. The FDIR recovery logic executes successfully as soon as the Vysochanskij-Petunin concentration inequality bounds are violated. This exercises Algorithm 1 in simulated flight, as an extension of the FDIR experiment done in Figure 9. Evidently, the relative position estimates continue meeting the sub-cm accuracy requirements despite a full cycle-slip event on all channels every orbit, at the expense of several minutes of invalid state estimation, due to the filter engaging in recovery.

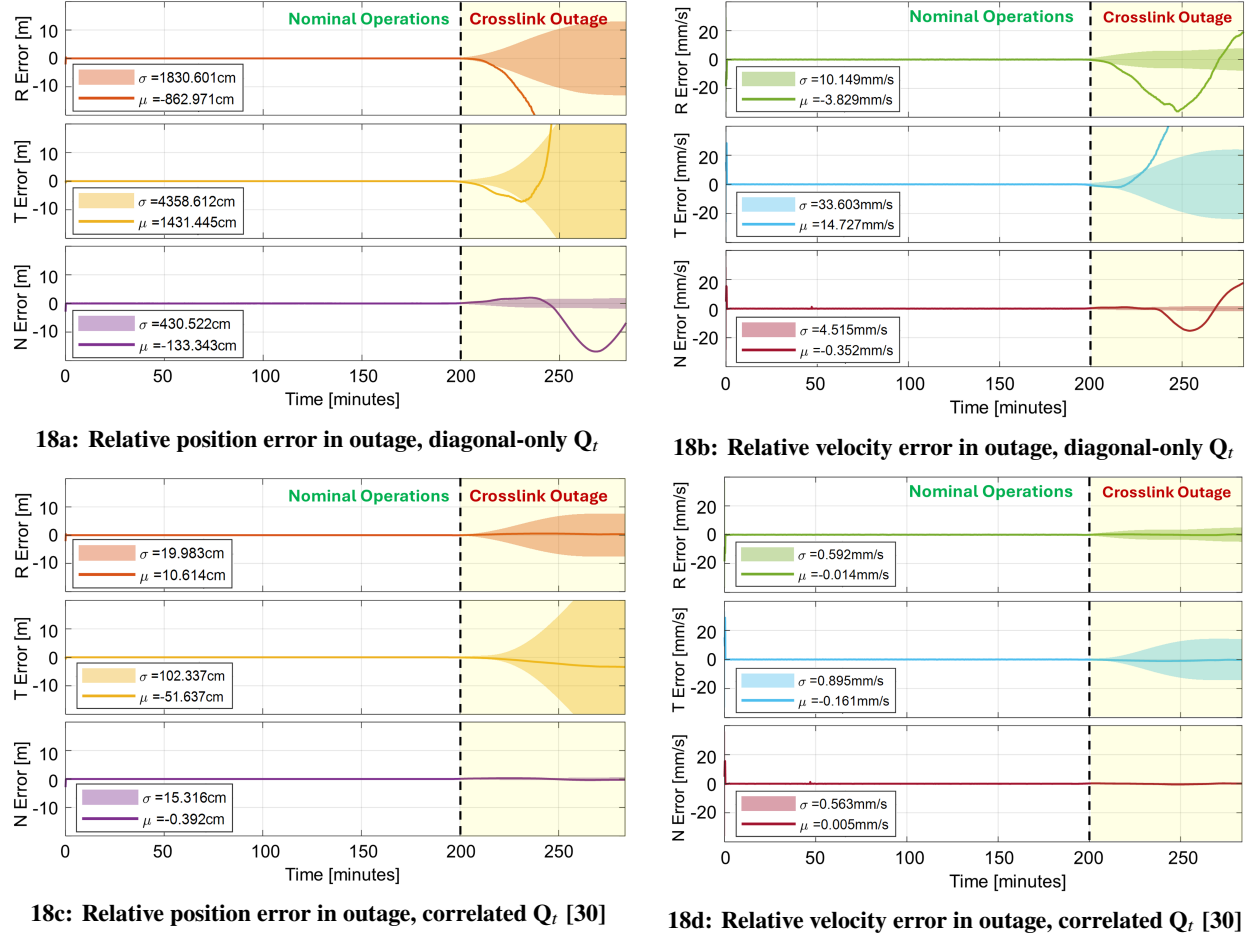


Fig. 18 Plots of relative navigation performance using the legacy manually tuned diagonal-only process noise in DiGiTaL v1 [20] (top), versus the proposed correlated analytical process noise model of DiGiTaL v2 (bottom).

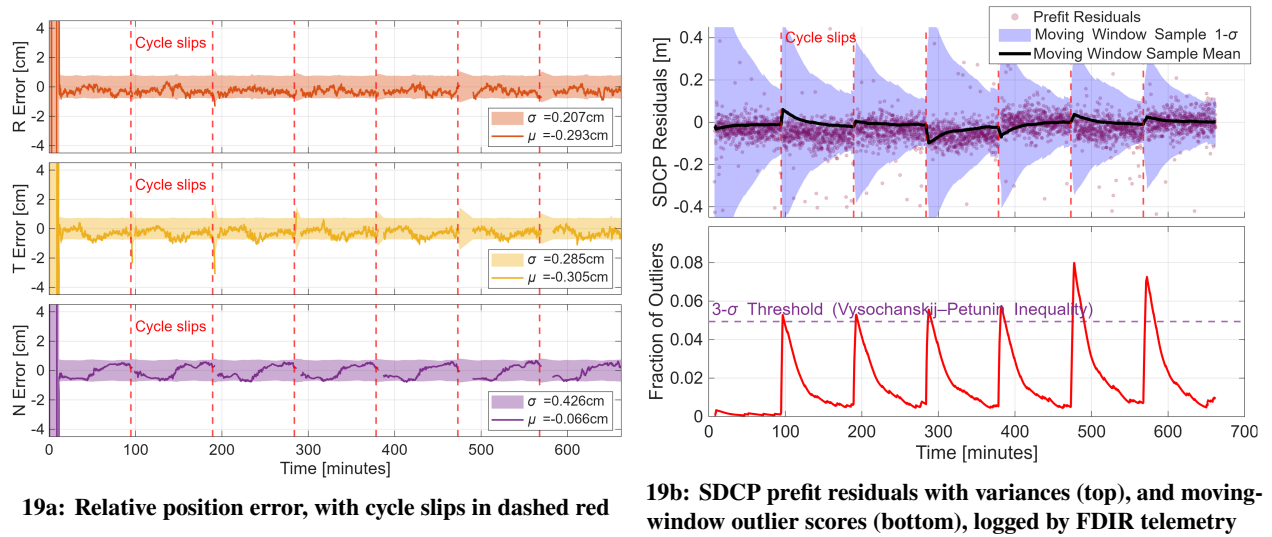


Fig. 19 Plots of relative navigation and FDIR performance, under full-cycle slip events once every orbit.

C. Comparative Performance and Runtime Analyses with Predecessor Software

A comparative analyses of performance (Table 15) and runtime (Table 16) was conducted between DiGiTaL v2 and its predecessor [21], using Test Campaign **T.3.2** and **T.4.1**. To ensure a fair ceteris paribus comparison between two versions of the software, *all* modeling parameters (dynamics, measurements, simulation environment) applied are identical to both. The same Mersenne Twister seeds are also applied in the simulation environment to ensure identical pseudorandom inputs that stimulate the flight software. The computer-under-test, which runs the flight software, is a *Xilinx Zynq-7000* System-on-Chip, an exact representation of the VISORS flight computer. It is a two-core embedded processor, ARM Cortex-A9, 650 MHz, where the operating system is PetaLinux 2016.2, running on Linux Kernel v4.4.

Table 15 Root-mean-square errors (RMSE) computed, with VISORS observation success rates, using legacy (v1) and improved (v2) filter designs. Outage scenario follows T.4.1, with RMSE computed during the outage.

	Filter Type	Abs. Pos. RMSE [meters]	Abs. Vel. RMSE [mm/s]	Rel. Pos. RMSE [mm]	Rel. Vel. RMSE [mm/s]	Rel. Pos. (outage) RMSE [m]	Rel. Vel. (outage) RMSE [mm/s]	VISORS Observation Success
DiGiTaL v1	EKF	12.409	15.561	1.828	0.041	55.838	45.802	1 / 10
	EKF-UKF Hybrid	10.388	13.551	1.820	0.041	53.436	44.745	1 / 10
DiGiTaL v2	Regularized CEKF (Joseph Form)	1.950	8.764	1.790	0.040	1.054	1.204	2 / 10
	Sparse Regularized CEKF (Non-Joseph-Form)	1.934	8.762	1.813	0.041	1.196	1.289	2 / 10

Table 16 Analyses of averaged runtimes, units in [ms] for core navigation function calls on the VISORS computers (Xilinx Zynq-7000 SoC). IAR runtime is recorded as the time of largest batch size to fix.

	Filter Type	Time Update [ms]	GRAPHIC [ms]	SDCP [ms]	IAR (max) [ms]	Total [ms]
DiGiTaL v1	EKF	1.384	14.284	14.697	0.861	31.226
	EKF-UKF Hybrid	1.386	20.806	34.226	0.863	57.281
DiGiTaL v2	Regularized CEKF (Joseph Form)	1.414	19.208	19.726	0.908	41.256
	Sparse Regularized CEKF (Non-Joseph-Form)	1.405	1.043	1.515	0.884	4.847

In terms of accuracy, the filter designs of DiGiTaL v2 exceed its predecessor in all areas in both nominal and off-nominal (outage) conditions. Significant improvements were observed in open-loop orbit prediction accuracy and absolute position estimation, by virtue of the improved process noise modeling. Marginal improvements were observed in relative state accuracy. In terms of runtime, a trade-off exists where the Sparse-Regularized CEKF in non-Joseph form is significantly faster and more memory-efficient but does not provide a mathematical guarantee on a positive definite state covariance. In contrast, the Joseph form does do so, but at the cost of significantly slower execution speed, comparable to its predecessor, because matrix terms in Joseph form are dense. This choice depends on the balance between efficiency and robustness. In light of this, the software has enabled a feature to toggle on or off the Joseph-form of the CEKF, via telecommands. Either way, runtimes still meet state update interval requirements for VISORS.

VII. Conclusion

This paper presents a complete CDGNSS-based navigation flight software package tailored for high-precision DSS missions. A rigorous, requirements-driven design process led to DiGiTaL v2, an end-to-end architecture emphasizing numerical stability, computational efficiency, and fault detection with isolation and recovery. The modular software framework and optimization strategies facilitate integration into emerging DSS host systems. Performance is validated through a multi-stage test campaign culminating in flight-like results from the VISORS mission. A carefully designed test campaign, with graduated fidelity, enables rapid failure point traceability via bisection. Comprehensive documentation of the design, development, and outcomes of this work aims to position the DiGiTaL v2 as a reference for emerging missions with stringent relative navigation needs. Viable research directions to improve the software in terms of scalability, robustness, and fault tolerance have been identified.

Acknowledgements: The authors gratefully acknowledge the support of the the NSF (Award No. 1936663), as well as DSO National Laboratories for fellowship support. The authors also extend their gratitude towards members of the VISORS team at large, as well as our reviewers: Adam Koenig (Relativity Space), Bo Naasz (NASA) and Christopher Roscoe (Ten One Aerospace).

References

- [1] D'Amico, S., "Autonomous Formation Flying in Low Earth Orbit," Ph.D. thesis, TU Delft, 2010.
- [2] Teunissen, P., "A new method for fast carrier phase ambiguity estimation," *Proceedings of 1994 IEEE Position, Location and Navigation Symposium-PLANS'94*, IEEE, 1994, pp. 562–573.
- [3] Kroes, R., Montenbruck, O., Bertiger, W., and Visser, P., "Precise GRACE baseline determination using GPS," *GPS Solutions*, Vol. 9, 2005, pp. 21–31.
- [4] Montenbruck, O., D'Amico, S., Ardaens, J.-S., and Wermuth, M., "Carrier phase differential GPS for LEO formation flying—the PRISMA and TanDEM-X flight experience," *Paper AAS*, 2011, pp. 11–489.
- [5] D'Amico, S., and Montenbruck, O., "Differential GPS: An enabling technology for formation flying satellites," *Small Satellite Missions for Earth Observation: New Developments and Trends*, Springer, 2010, pp. 457–465.
- [6] D'Amico, S., Ardaens, J.-S., and De Florio, S., "Autonomous formation flying based on GPS - PRISMA flight results," *Acta Astronautica*, Vol. 82, No. 1, 2013, pp. 69–79. <https://doi.org/https://doi.org/10.1016/j.actaastro.2012.04.033>, 6th International Workshop on Satellite Constellation and Formation Flying.
- [7] Roth, N. H., "Navigation and Control Design for the CanX-4/-5 Satellite Formation Flying Mission," Ph.D. thesis, University of Toronto, 2010.
- [8] Kahr, E., Roth, N., Montenbruck, O., Risi, B., and Zee, R. E., "GPS Relative Navigation for the CanX-4 and CanX-5 Formation-Flying Nanosatellites," *Journal of Spacecraft and Rockets*, Vol. 55, No. 6, 2018, pp. 1545–1558. <https://doi.org/10.2514/1.A34117>.
- [9] Koenig, A., D'Amico, S., and Lightsey, E. G., *Formation Flying Orbit and Control Concept for the VISORS Mission*, AIAA, 2021, Chap. 0, p. 0. <https://doi.org/10.2514/6.2021-0423>.
- [10] Guffanti, T., Bell, T., Low, S. Y. W., Murray-Cooper, M., and D'Amico, S., "Autonomous Guidance, Navigation and Control of the VISORS Formation Flying Mission," *AAS/AIAA Astrodynamics Specialist Conference*, Big Sky, Montana, 2023, p. 0.
- [11] Giraldo, V., and D'Amico, S., "Precise real-time relative orbit determination for large-baseline formations using GNSS," *Proceedings of the 2021 International Technical Meeting of The Institute of Navigation*, 2021, pp. 366–384.
- [12] Koenig, A. W., D'Amico, S., Macintosh, B., and Titus, C. J., "Formation design analysis for a miniaturized distributed occulter/telescope in earth orbit," *International Symposium on Space Flight Dynamics (ISSFD)*, DLR German Space Operations Center and the European Space Agency, 2015.
- [13] Macintosh, B., D'Amico, S., Koenig, A., Bendek, E., Grogran, K., Shaklan, S., Madurowicz, A., de Rosa, R., Greene, T., Debes, J., Douglas, E., Jensen-Clem, R., Duchene, G., and Esposito, T., "Miniature Distributed Occulter Telescope (mDOT) Publicly Released Project Report," Tech. rep., Stanford University, Space Rendezvous Laboratory, 2022.
- [14] Monnier, J. D., Jain, P., Kalluri, S., Cutler, J., D'Amico, S., Lightsey, G., Pogorelyuk, L., Vasisht, G., Cahoy, K., and Meyer, M., "STARI: starlight acquisition and reflection toward interferometry," *Space Telescopes and Instrumentation 2024: Optical, Infrared, and Millimeter Wave*, Vol. 13092, SPIE, 2024, pp. 1095–1107.
- [15] Ito, T., Izumi, K., Kawano, I., Funaki, I., Sato, S., Akutsu, T., Komori, K., Musha, M., Michimura, Y., Satoh, S., et al., "SILVIA: Ultra-precision formation flying demonstration for space-based interferometry," *arXiv preprint arXiv:2504.05001*, 2025.
- [16] Corazzini, T., Robertson, A., Adams, J. C., Hassibi, A., and How, J. P., "GPS sensing for spacecraft formation flying," *Proceedings of the 10th International Technical Meeting of the Satellite Division of The Institute of Navigation (ION GPS 1997)*, 1997, pp. 735–744.
- [17] Inalhan, G., Busse, F. D., and How, J. P., "Precise formation flying control of multiple spacecraft using carrier-phase differential GPS," *AAS/AIAA Space Flight Mechanics Meeting, Clearwater, FL*, 2000, pp. 23–26.
- [18] Scala, F., Colombo, C., Gaias, G., Martin-Neira, M., et al., "GNSS-based navigation for a remote sensing three-satellite formation flying," *SpaceOps 2021 Virtual Edition*, 16th International Conference on Space Operations, 2021, pp. 1–18.
- [19] Shim, H., Kim, O.-J., Yu, S., Kee, C., Cho, D.-H., and Kim, H.-D., "Precise in-orbit relative navigation technique for rendezvous mission of CubeSats using only GPS receivers," *CEAS Space Journal*, Vol. 16, No. 1, 2024, pp. 117–137.
- [20] Giraldo, V. P., and D'Amico, S., "Distributed multi-GNSS timing and localization for nanosatellites," *NAVIGATION*, Vol. 66, No. 4, 2019, pp. 729–746. <https://doi.org/10.1002/navi.337>.
- [21] Giraldo, V. P., "Precision Navigation of Miniaturized Distributed Space Systems using GNSS," Ph.D. thesis, Stanford University, 2021.
- [22] Kruger, J. J., Guffanti, T., Park, T. H., Murray-Cooper, M., Low, S. Y., Bell, T., D'Amico, S., Roscoe, C. W., and Westphal, J., "Adaptive End-to-End Architecture for Autonomous Spacecraft Navigation and Control During Rendezvous and Proximity Operations," *AIAA SCITECH 2024 Forum*, 2024, p. 0430.
- [23] Low, S. Y., and D'Amico, S., "Precise Distributed Satellite Navigation: Differential GPS with Sensor-Coupling for Integer Ambiguity Resolution," *2024 IEEE Aerospace Conference*, IEEE, 2024, pp. 1–18.
- [24] Low, S., and Kochenderfer, M., "Optimal Pointing Sequences in Spacecraft Formation Flying using Online Planning with Resource Constraints," *Learning for Dynamics and Control Conference*, PMLR, 2022, pp. 355–365.
- [25] D'Amico, S., Ardaens, J.-S., and Larsson, R., "Spaceborne Autonomous Formation-Flying Experiment on the PRISMA Mission," *Journal of Guidance, Control, and Dynamics*, Vol. 35, No. 3, 2012, pp. 834–850. <https://doi.org/10.2514/1.55638>.
- [26] Kornfeld, R. P., Arnold, B. W., Gross, M. A., Dahya, N. T., Klipstein, W. M., Gath, P. F., and Bettadpur, S., "GRACE-FO: The Gravity Recovery and Climate Experiment Follow-On Mission," *Journal of Spacecraft and Rockets*, Vol. 56, No. 3, 2019, pp. 931–951. <https://doi.org/10.2514/1.A34326>.
- [27] Xia, Y., Liu, X., Guo, J., Yang, Z., Qi, L., Ji, B., and Chang, X., "On GPS data quality of GRACE-FO and GRACE satellites: Effects of phase center variation and satellite attitude on precise orbit determination," *Acta geodaetica et geophysica*, Vol. 56, 2021, pp. 93–111.
- [28] Bowen, J., Tsuda, A., Abel, J., and Villa, M., "Cubesat proximity operations demonstration (cpod) mission update," *2015 IEEE Aerospace Conference*, IEEE, 2015, pp. 1–8.
- [29] Roscoe, C. W., Westphal, J. J., and Mosleh, E., "Overview and GNC design of the CubeSat Proximity Operations Demonstration (CPOD) mission," *Acta Astronautica*, Vol. 153, 2018, pp. 410–421.

- [30] Llorente, J. S., Agenjo, A., Carrascosa, C., de Negueruela, C., Mestreau-Garreau, A., Cropp, A., and Santovincenzo, A., "PROBA-3: Precise formation flying demonstration mission," *Acta Astronautica*, Vol. 82, No. 1, 2013, pp. 38–46.
- [31] Ardaens, J.-S., D'Amico, S., and Cropp, A., "GPS-based relative navigation for the Proba-3 formation flying mission," *Acta Astronautica*, Vol. 91, 2013, pp. 341–355.
- [32] Enderle, W., Gini, F., Schönmann, E., and Mayer, V., "Proba-3 precise orbit determination based on GNSS observations," *Proceedings of the 32nd International Technical Meeting of the Satellite Division of The Institute of Navigation (ION GNSS+ 2019)*, 2019, pp. 1187–1198.
- [33] Hwang, J. W., Shim, H., Bae, Y., Kee, C., and Kim, J., "Propellant-Free Rendezvous Mission of SNUGLITE-III CubeSat: Orbit Control Using Aerodynamic Forces," *2025 IEEE Aerospace Conference*, IEEE, 2025, pp. 1–12.
- [34] Shim, H., and Kee, C., "Highly Efficient Real-Time Kinematic-Based Precise Relative Navigation for Autonomous Rendezvous CubeSat," *NAVIGATION: Journal of the Institute of Navigation*, Vol. 71, No. 3, 2024.
- [35] Monnier, J. D., et al., "A realistic roadmap to formation flying space interferometry," *arXiv preprint arXiv:1907.09583*, 2019.
- [36] Kapurch, S. J., *NASA systems engineering handbook*, Diane Publishing, 2010.
- [37] Koenig, A. W., and D'Amico, S., "Robust and Safe N-Spacecraft Swarming in Perturbed Near-Circular Orbits," *Journal of Guidance, Control, and Dynamics*, Vol. 41, No. 8, 2018, pp. 1643–1662. <https://doi.org/10.2514/1.G003249>.
- [38] Giraldo, V. P., Chernick, M., and D'Amico, S., "Guidance, navigation, and control for the DWARF formation-flying mission," *AAS/AIAA Astrodynamics Specialist Conference, South Lake Tahoe, CA*, 2020, p. 0.
- [39] Enge, P. K., and Misra, P., *The Global Positioning System: Signals, Measurements, and Performance (Second Edition)*, Ganga-Jamuna Press, 2006.
- [40] Shoemake, K., "Animating rotation with quaternion curves," *Proceedings of the 12th annual conference on Computer graphics and interactive techniques*, 1985, pp. 245–254.
- [41] Psiaki, M. L., and Mohiuddin, S., "Modeling, Analysis, and Simulation of GPS Carrier Phase for Spacecraft Relative Navigation," *Journal of Guidance, Control, and Dynamics*, Vol. 30, No. 6, 2007, pp. 1628–1639. <https://doi.org/10.2514/1.29534>.
- [42] Gutsche, K., Hobiger, T., and Winkler, S., "Addressing Inaccurate Phase Center Offsets in Precise Orbit Determination for Agile Satellite Missions," *NAVIGATION: Journal of the Institute of Navigation*, Vol. 71, No. 4, 2024.
- [43] Lowe, S., Markevitch, M., and D'Amico, S., "Relative navigation and pointing error budget for an x-ray astronomy formation-flying mission," *Proceedings of the 44th Annual American Astronautical Society Guidance, Navigation, and Control Conference*, 2022, Springer, 2022, pp. 1433–1445.
- [44] Zanetti, R., DeMars, K. J., and Bishop, R. H., "Underweighting Nonlinear Measurements," *Journal of Guidance, Control, and Dynamics*, Vol. 33, No. 5, 2010, pp. 1670–1675. <https://doi.org/10.2514/1.50596>.
- [45] Carpenter, J. R., and D'souza, C. N., "Navigation filter best practices," Tech. rep., NASA, 2018.
- [46] Schmidt, S. F., "Application of state-space methods to navigation problems," *Advances in control systems*, Vol. 3, Elsevier, 1966, pp. 293–340.
- [47] Jazwinski, A. H., *Stochastic processes and filtering theory*, Academic Press, Inc., 1970.
- [48] Woodbury, D., and Junkins, J., *On the Consider Kalman Filter*, AIAA, 2010, Chap. 0, p. 0. <https://doi.org/10.2514/6.2010-7752>.
- [49] Schlee, F. H., Standih, C. J., and Toda, N. F., "Divergence in the Kalman filter," *AIAA Journal*, Vol. 5, No. 6, 1967, pp. 1114–1120. <https://doi.org/10.2514/3.4146>.
- [50] Yunck, T. P., "Coping with the atmosphere and ionosphere in precise satellite and ground positioning," *Washington DC American Geophysical Union Geophysical Monograph Series*, Vol. 73, 1993, pp. 1–16.
- [51] Low, S. Y., and D'Amico, S., "The Consider Kalman Filter in Joseph Form," Stanford Space Rendezvous Laboratory, 2025. Internal technical note.
- [52] Stacey, N., and D'Amico, S., "Adaptive and dynamically constrained process noise estimation for orbit determination," *IEEE Transactions on Aerospace and Electronic Systems*, Vol. 57, No. 5, 2021, pp. 2920–2937.
- [53] Montenbruck, O., and Gill, E., *Satellite Orbits: Models, Methods and Applications*, Springer, 2010.
- [54] Carpenter, J. R., and Alfried, K. T., "Navigation accuracy guidelines for orbital formation flying," *The Journal of the Astronautical Sciences*, Vol. 53, 2005, pp. 207–219.
- [55] How, J. P., Breger, L. S., Mitchell, M., Alfried, K. T., and Carpenter, R., "Differential semimajor axis estimation performance using carrier-phase differential global positioning system measurements," *Journal of guidance, control, and dynamics*, Vol. 30, No. 2, 2007, pp. 301–313.
- [56] Gallager, R. G., *Stochastic processes: theory for applications*, Cambridge University Press, 2013.
- [57] Stacey, N., and D'Amico, S., "Analytical process noise covariance modeling for absolute and relative orbits," *Acta Astronautica*, Vol. 194, 2022, pp. 34–47.
- [58] Chang, X. W., Yang, X., and Zhou, T., "MLAMBDA: A modified LAMBDA method for integer least-squares estimation," *Journal of Geodesy*, Vol. 79, 2005, pp. 552–565.
- [59] Teunissen, P., "The invertible GPS ambiguity transformations," *Manuscripta Geodetica*, Vol. 20, 1995, pp. 489–497.
- [60] Teunissen, P., "Success probability of integer GPS ambiguity rounding and bootstrapping," *Journal of geodesy*, Vol. 72, 1998, pp. 606–612.
- [61] Teunissen, P. J., and Odijk, D., "Ambiguity dilution of precision: definition, properties and application," *Proceedings of the 10th International Technical Meeting of the Satellite Division of The Institute of Navigation (ION GPS 1997)*, 1997, pp. 891–899.
- [62] Vysochanskij, D., and Petunin, Y. I., "Justification of the 3σ rule for unimodal distributions," *Theory of Probability and Mathematical Statistics*, Vol. 21, No. 25-36, 1980.
- [63] Pukelsheim, F., "The three sigma rule," *The American Statistician*, Vol. 48, No. 2, 1994, pp. 88–91.
- [64] Bell, T., and D'Amico, S., "Event-Driven Simulation for Rapid Iterative Development of Distributed Space Flight Software," *2025 IEEE Aerospace Conference*, IEEE, 2025.